

Forecasts on Primordial non-Gaussianity from 21 cm Intensity Mapping experiments

Dionysios Karagiannis,^{a,c,1} Anže Slosar,^b Michele Liguori,^{a,c}

^aDipartimento di Fisica e Astronomia “G. Galilei”, Università degli Studi di Padova, via Marzolo 8, I-35131, Padova, Italy

^bPhysics Department, Brookhaven National Laboratory, Upton, NY 11973, USA

^cINFN, Sezione di Padova, via Marzolo 8, I-35131, Padova, Italy

E-mail: dakaragian@gmail.com

Abstract. We forecast the ability of dedicated 21 cm intensity mapping experiments to constraint primordial non-Gaussianity using power spectrum and bispectrum. We model the signal by including the non-linear biasing expansion through a generalized halo model approach. We consider the importance of foreground filtering scale and of the foreground wedge. We find that the current generation intensity mapping experiments like CHIME do not possess sufficient sensitivity to be competitive with the existing limits. On the other hand, upcoming experiments like HIRAX can improve the current constraints and the proposed PUMA experiment can substantially improve them, reaching sensitivities below $\sigma(f_{\text{NL}}) < 5$ for equilateral and orthogonal configurations and $\sigma(f_{\text{NL}}) < 1$ for the local shape, if good foreground control is achieved.

¹Corresponding author.

Contents

1	Introduction	1
2	Modeling the signal	3
2.1	Matter power spectrum and bispectrum	3
2.2	Halo bias and Mass function	4
2.3	HI bias	6
2.4	Power spectrum and bispectrum of HI in redshift space	8
3	Modeling the thermal noise of 21 cm surveys	9
3.1	Foreground exclusions	10
4	Fisher Matrix Analysis	11
5	Results	14
6	Conclusions	18
A	Derivation of Bias Parameters from the Tinker et al mass function with the PBS approach	28
B	Baseline distribution	29
C	Redshift space kernels and the Finger-of-God dumping term	31

1 Introduction

Understanding primordial cosmological inflation in detail is one of the biggest challenges of modern physics. Currently, inflation is essentially a generic framework for setting up the hot big bang, rather than a concrete, specific theory: any scalar field rolling down a sufficiently flat potential will produce a nearly spatially flat universe with small seed fluctuations which allow the hot Big Bang to proceed and eventually create the universe as we know it. Nevertheless, we do have a few observational handles that help us to distinguish between a simplest realization of inflation – that is, a minimal single-field scenario – and more complex models, such as those involving multiple fields and non-minimal couplings. A convincing detection in any of these probes of non canonical physics will be crucial in connecting inflation to the bigger puzzle of fundamental physics.

Primordial non-Gaussianity (PNG) has emerged as one such powerful probe in the last decade [1, 2]. In the simplest models of inflation, containing a single scalar field, the resulting fluctuations in the curvature field are nearly perfectly Gaussian, essentially encoding the physics of the lowest energy state of a quantized scalar field. This picture breaks, if there are either multiple interacting fields involved in inflation, or non-minimal couplings of the inflaton, or if slow-roll is broken [3–12] (see also Refs. [2, 13, 14] for a general review and discussion). Since we know that the primordial fluctuations *are* Gaussian to a very good degree, these effects must be perturbative. As a result, in most scenarios, a non-zero three-point function is generated at leading order in a cumulant expansion of the primordial curvature fluctuation

field. Resulting bi-spectra are classified by the shape of the triangle configurations that dominate the signal, as we will discuss in more detail in the next section. Needless to say, a detection of this signal would bear far-reaching theoretical implications and be of paramount importance in cosmology.

Measurements of the very small non-Gaussianity signal are difficult and dominated by the sample variance of the observable, i.e. by the number of modes which can be used to measure any deviation from zero bi-spectrum. Currently, the most competitive constraints come from CMB observations [15]. However, the constraints derived from the Large Scale Structure (LSS) are catching up fast [16–21]. In fact, due to its inherently three-dimensional structure and thus a larger number of measured linear modes, LSS is expected to soon supersede CMB measurements [21, 22].

In light of this premise, we investigate here the possibility of 21 cm intensity mapping (IM) observations to probe primordial non-Gaussianity. More specifically, we develop the methodology to perform non-Gaussianity forecasts for intensity mapping surveys, and apply it to current and proposed experiments. Developments in technology and in our understanding of the signal have recently allowed proposing very ambitious experimental designs in this area, which can still be implemented at reasonable cost. For example, PUMA [23] will observe the low-redshift universe from $z = 0.3$ to $z = 6$, with a single instrument over approximately half the sky. This extremely large volume suggests the possibility that intensity mapping will be at least competitive with the CMB in placing primordial non-Gaussianity constraints.

The forthcoming Square Kilometer Array (SKA) [24] neutral hydrogen survey is expected to probe the cosmological HI signal over 3/4 of the sky, for a wide range of redshifts, allowing us to push below the Planck constraints on PNG [25]. In addition, the SKA phase 1, with its large volume and wide frequency range, could in principle produce competitive constraints on the local PNG, where uncertainties of $\sigma(f_{\text{NL}}^{\text{loc}}) \approx 1 - 4$ are considered to be achievable [24–27]. These approaches utilise the large scale power excess, induced by PNG, in the power spectrum of biased tracers [16, 28–31] and treat SKA1 as a set of single dishes [32], while consider an effective treatment of the foregrounds (see Refs. [27, 33] for a discussion). These constraints could be pushed even further by taking into advantage the multitracer technique [34, 35]. In Ref. [36], they use the Tianlai cylinder array [37] to present forecasts on PNG from both power spectrum and bispectrum, where they assume a rather simple model for the latter. Here we adopt the complete model, up to tree-level, for the redshift space HI power spectrum and bispectrum, while we take into account theoretical limitations and a variety of observational effects (see Ref. [22] for an extensive discussion). Adding to this, a careful treatment of foreground systematics is applied, providing realistic forecasts on the amplitude of PNG.

We note here that it might seem fanciful to make forecasts for the ability of 21 cm experiments to measure non-Gaussianity, when we do not even have basic clean auto-power spectrum measurements from observations of 21 cm intensity maps, let alone baryon acoustic oscillation measurements. However, we note that the current observational issues are entirely due to imperfect calibration and stability of the instrument, rather than being of fundamental astrophysical nature. Therefore, the approach we take is to forecast the statistical sensitivity to non-Gaussianity in the presence of irreducible systematic issues such as foreground contamination, assuming that purely instrumental issues will be solved in time. In fact, the competitive figures that we find should provide additional impetus for the R&D that is required to make the 21 cm observations a success.

This paper is structured as follows. In Section 2 we present our model for the large-scale

fluctuations of the neutral hydrogen density. In Section 3 we discuss observational limitations and specifications of three experiments under consideration in this paper, while in Section 4 we present the Fisher matrix formalism used to forecast the amplitude of PNG. We present our results in Section 5, followed by Conclusions (Section 6).

2 Modeling the signal

2.1 Matter power spectrum and bispectrum

The two point statistics of the primordial curvature perturbation field in Fourier space, $\zeta(\mathbf{k})$, is defined as

$$\langle \zeta(\mathbf{k})\zeta(\mathbf{k}') \rangle = (2\pi)^3 \delta_D(\mathbf{k} - \mathbf{k}') P_\zeta(\mathbf{k}). \quad (2.1)$$

These primordial perturbations, generated through inflation, are nearly perfectly Gaussian. Therefore, they can be characterized by the two-point correlation function. They are also directly related to the Bardeen gauge invariant primordial gravitational potential $\Phi(\mathbf{k})$ (during matter domination era, $\Phi(\mathbf{k}) = 3/5\zeta(\mathbf{k})$), which is in turn related, through the cosmological Poisson equation, to the linearly evolved dark matter density contrast $\delta_m^L(\mathbf{k}, z) = M(k, z)\Phi(k)$. The linear matter power spectrum is thus defined, as

$$P_m^L(k, z) = M^2(k, z)P_\Phi(k), \quad (2.2)$$

where

$$M(k, z) = \frac{2k^2 c^2 T(k) D(z)}{3\Omega_m H_0^2}. \quad (2.3)$$

In the above equation, $D(z)$ is the linear growth factor, originating from the growing mode of the linear fluid equations, normalised to unity today (i.e. $D(0) = 1$). $T(k)$ is the matter transfer function normalized to unity at large scales ($k \rightarrow 0$) and c is the speed of light. In this work, we use *Planck* 2015 best-fit parameters [38] to define the fiducial cosmology used to derive the matter power spectrum, which is computed with the numerical Boltzmann code CAMB [39].

Various inflationary theories predict a small deviation from perfectly Gaussian initial conditions. This leads to non-zero high-order correlation functions of the curvature perturbation field. The largest of such correlators – in Fourier space – is in most cases the bispectrum, i.e., the three-point correlation function of Fourier modes, defined as:

$$\langle \zeta(\mathbf{k}_1)\zeta(\mathbf{k}_2)\zeta(\mathbf{k}_3) \rangle = (2\pi)^3 \delta_D(\mathbf{k}_1 + \mathbf{k}_2 + \mathbf{k}_3) B_\zeta(\mathbf{k}_1, \mathbf{k}_2, \mathbf{k}_3). \quad (2.4)$$

The strength of the bispectrum signal is generally described by a dimensionless amplitude parameter, called f_{NL} . In addition to this, the Dirac delta (enforcing homogeneity) imposes a dependence of the bispectrum on the shape of the different Fourier space triangles. Following the equations above, we can write, at leading order, the linearly extrapolated PNG contribution of the matter density bispectrum as:

$$B_I(k_1, k_2, k_3, z) = M(k_1, z)M(k_2, z)M(k_3, z)B_\Phi(k_1, k_2, k_3) \quad (2.5)$$

where B_Φ , as in the case of the power spectrum, is related to B_ζ through the Poisson equation and therefore provides a window to the non-linear interaction during inflation. The number

of shapes of the forming triangles is large and the different inflation models predict PNG that picks at different configurations. In this work, we will consider three very important shapes of PNG, namely the *local* shape [40–43], the *equilateral shape* [44] and the *orthogonal* [45], defined respectively as:

$$B_{\Phi}^{\text{loc}}(k_1, k_2, k_3) = 2f_{\text{NL}}^{\text{loc}} [P_{\Phi}(k_1)P_{\Phi}(k_2) + 2 \text{ perms}] , \quad (2.6)$$

$$B_{\Phi}^{\text{eq}}(k_1, k_2, k_3) = 6f_{\text{NL}}^{\text{equil}} \left[- [P_{\Phi}(k_1)P_{\Phi}(k_2) + 2 \text{ perms}] - 2[P_{\Phi}(k_1)P_{\Phi}(k_2)P_{\Phi}(k_3)]^{2/3} + [P_{\Phi}^{1/3}(k_1)P_{\Phi}^{2/3}(k_2)P_{\Phi}(k_3) + 5 \text{ perms}] \right] , \quad (2.7)$$

$$B_{\Phi}^{\text{orth}}(k_1, k_2, k_3) = 6f_{\text{NL}}^{\text{orth}} \left[3[P_{\Phi}^{1/3}(k_1)P_{\Phi}^{2/3}(k_2)P_{\Phi}(k_3) + 5 \text{ perms}] - 3[P_{\Phi}(k_1)P_{\Phi}(k_2) + 2 \text{ perms}] - 8(P_{\Phi}(k_1)P_{\Phi}(k_2)P_{\Phi}(k_3))^{2/3} \right] . \quad (2.8)$$

The signal of these templates peaks at the squeezed triangles ($k_3 \ll k_2 \simeq k_1$), the equilateral configurations ($k_3 \simeq k_2 \simeq k_1$) and in both equilateral and folded triangles ($k_1 \simeq k_2 \simeq k_3/2$), respectively.

Due to the non-linear nature of gravity, the matter bispectrum has additional terms at the zeroth-order (tree-level). Therefore, measuring the amplitude of PNG from the bispectrum of LSS is a highly non-trivial process. Robust modelling of non-linearities should be considered, in order to remove these gravitational contaminants and retrieve a clear PNG signal. Here, we account for the gravity induced non-linearities in the framework of Standard Perturbation Theory (SPT) [e.g. see Ref. [46] for a review]. Through out this work, we will restrict our analysis up to linear/semi-nonlinear scales, in order to be consistent with the SPT approach. Thus, we will only use the linear power spectrum and the tree-level bispectrum in SPT (see Sec. 2.4).

2.2 Halo bias and Mass function

The measurement of PNG from the LSS of the Universe requires a robust description of the relation between the dark matter haloes and the underlying matter distribution. The connection between the two is incorporated under the concept of *bias*. A perturbative approach has been used in the past to describe the halo bias, by expanding the halo over-density field δ_h in powers of δ_m [47–50], while tidal field terms were added in the expansion later on [51–55]. A complete set of bias terms was derived in Refs. [56–58], where δ_h is expanded over renormalised operators that incorporate all possible local gravitational observables, like δ_m or the tidal field $s_{ij} = (\partial_i \partial_j / \nabla^2 - \delta_{ij}/3)\delta_m$. In this *general bias* expansion and for Gaussian initial conditions, the terms up to second order (needed for the tree-level bispectrum) can be written in the Eulerian framework as [56–58]:

$$\delta_h^{E,(G)}(\mathbf{x}, \tau) = b_1^E(\tau)\delta(\mathbf{x}, \tau) + \varepsilon^E(\mathbf{x}, \tau) + \frac{b_2^E(\tau)}{2}\delta^2(\mathbf{x}, \tau) + \frac{b_{s^2}^E(\tau)}{2}s^2(\mathbf{x}, \tau) + \varepsilon_{\delta}^E(\mathbf{x}, \tau)\delta(\mathbf{x}, \tau) , \quad (2.9)$$

where τ is the conformal time and \mathbf{x} are the spatial co-moving coordinates in the Eulerian frame. In addition, $s^2 = s_{ij}s^{ij}$ is the simplest scalar that can be formed by the tidal field, ε^E is the leading stochastic bias contribution [59–61] and ε_{δ}^E is the stochastic counterpart of the linear bias. For the scales considered here, i.e. much larger scales than those involved in the halo formation, where the perturbative description breaks down, the terms in Eq. (2.9) are

sufficient to describe the halo statistics. This means that, the higher-order derivative contribution, which become important towards the halo formation scales, can be safely excluded (see Refs. [62, 63] for the full modeling and extensive discussion). The second-order tidal field bias coefficient, following the convention of Ref. [55], is given by $b_{s_2}^E = -4/7(b_1^E - 1)$. This relation assumes the Lagrangian tidal bias to be $b_{s_2}^L = 0$, as well as a convolution of matter and tracer. It is tested against numerical results in Ref. [64], where they find it to be a good approximation with an evidence of a small negative Lagrangian bias, i.e. $b_{s_2}^L < 0$.

The presence of PNG introduces a scale-dependent bias correction to the linear bias, originating from the coupling between the long-wavelength fluctuations and the small scales, which in turn is induced by the presence of the primordial bispectrum in the squeezed limit. This effect was studied extensively for local PNG [16, 28–31, 65], whose template peaks in the squeezed triangle configurations. Taking the squeezed limit of the bispectrum, in the case of a general non-local quadratic non-Gaussianity (e.g. equilateral PNG), also generates a scale-dependent bias correction [66–69]. In order to model this effect into the general bias description, an additional field Ψ is added (in the same spirit as in Refs. [70–72]) in the expansion. The full set of terms in the Eulerian framework for an arbitrary quadratic PNG up to second order in perturbations and linear in f_{NL} is [73]:

$$\delta_h^{E,(NG)}(\mathbf{x}, \tau) = b_{\Psi}^E(\tau)\Psi(\mathbf{q}) + b_{\Psi\delta}^E(\tau)\Psi(\mathbf{q})\delta(\mathbf{x}, \tau) + \varepsilon_{\Psi}^E(\mathbf{x}, \tau)\Psi(\mathbf{q}), \quad (2.10)$$

where \mathbf{q} are the spatial coordinates in the Lagrangian frame. The field Ψ is a non-local transformation of the Bardeen gravitational potential, given by $\Psi(\mathbf{q}) = \int d^3\mathbf{k} k^\alpha \Phi(\mathbf{k}) \exp(i\mathbf{k}\mathbf{q})$, where α takes real values, which depend on the PNG type considered (see Ref. [62] for an extensive discussion). Furthermore, ε_{Ψ}^E is the stochastic counterpart of the field Ψ .

The bias coefficients of the general bias expansion [Eqs. (2.9) and (2.10)], including those of the field Ψ (i.e. b_{Ψ} and $b_{\Psi\delta}$) can be derived by utilising the peak-background split (PBS) argument (see Appendix A for a quick review). The halo mass function, which is the mean co-moving number density of halos per logarithmic mass interval, can be parametrised in the form of [74]

$$n_h(M, z) = \frac{\bar{\rho}_m}{M} f(\nu) \left| \frac{d \ln \nu}{d \ln M} \right|, \quad (2.11)$$

where $\rho_m(z) = \Omega_m(z)\rho_c^0$ is the mean co-moving density at redshift z and ρ_c^0 is the critical density of the Universe at $z = 0$. The multiplicity function $f(\nu)$ is an arbitrary function of the peak height $\nu \equiv \delta_c/\sigma_R(M, z)$, while $\delta_c = 1.686$ is the threshold value needed for a dark matter peak to form a halo and $\sigma_R^2(M, z)$ is the variance of the linear density field smoothed with a top-hat filter over a radius R and enclosed mass $M = (4\pi/3)\bar{\rho}_m R^3$. In this work, for the theoretical halo mass function we will use the best-fit results, originating from the comparison to N-body simulations, presented in Ref. [75] (hereafter T08) and shown in Eq. (A.4).

For a universal mass function, like the one used here, analytic expressions can be derived for the non-Gaussian bias coefficients in Eulerian framework, after using the peak-background split bias parameters definition [Eq. (A.3)], which are given by [62, 69, 76]:

$$b_{\Psi}^E(M, z) = Af_{\text{NL}} \left[2\delta_c b_1^L + 4 \left(\frac{d \ln \sigma_{R,-\alpha}^2}{d \ln \sigma_R^2} - 1 \right) \right] \frac{\sigma_{R,-\alpha}^2}{\sigma_R^2}, \quad (2.12)$$

and [22, 71]

$$b_{\Psi\delta}^E(M, z) = 2Af_{\text{NL}} \left[\delta_c \left(b_2^E + \frac{13}{21}(b_1^E - 1) \right) + b_1^E \left(2 \frac{d \ln \sigma_{R,-\alpha}^2}{d \ln \sigma_R^2} - 3 \right) + 1 \right] \frac{\sigma_{R,-\alpha}^2}{\sigma_R^2},$$

where $\sigma_{R,n}^2 = 1/(2\pi)^3 \int d^3\mathbf{k} k^n W_R(k)^2 P^L(k, z)$, with W_R being the top-hat filter, while the superscript L and E over the bias correspond to the parameters in the Lagrangian and Eulerian framework respectively. For the details of deriving Eqs. (2.12) and (2.13), the reader is encouraged to check Appendix C of Ref. [22] or the discussion of Ref. [62]. The values of A and α depend on the PNG type considered, e.g. for the local case, $\alpha = 0$ and $A = 1$, these expressions reduce to the well known results $b_{\Psi}^E \rightarrow b_{\Phi}^E = 2f_{\text{NL}}^{\text{loc}} \delta_c b_1^L$ [16, 28, 71] and $b_{\Psi\delta}^E \rightarrow b_{\Phi\delta}^E = 2f_{\text{NL}}^{\text{loc}} [\delta_c b_2^E + (13/21\delta_c - 1)(b_1^E - 1)]$ [71, 72, 77]. In the cases of equilateral and orthogonal PNG, the values are $\alpha = 2$ and $A = 3$ and $\alpha = 1$ and $A = -3$ respectively [66, 78]. Note that, for the equilateral PNG ($\alpha = 2$), the scale-dependent bias correction, $b_{\Psi} k^\alpha / M(k)$ [Eq. (C.1)], approaches a constant value towards the large scales and thus becomes scale-independent. This creates strong degeneracies between $f_{\text{NL}}^{\text{equil}}$ and the linear bias coefficient b_1 , excluding the possibility of constraining equilateral PNG from the non-Gaussian bias term. Moreover, the transfer function present in $M(k)$, which produces a scale-dependence towards the small scales, introduces another degeneracy, this time between the PNG bias contribution and higher-order derivative bias terms. The presence of these degeneracies, on both large and small scales, indicate that the power spectrum does not essentially bear any constraining power on equilateral PNG [73]. Therefore, in the case of equilateral PNG, the forecasts coming from the two-point correlator are excluded from our analysis (see Sec. 5).

The presence of PNG introduces an additional scale-independent correction to the bias, due to the non-Gaussian correction to the mass function [79]. In Refs. [77, 80] these offsets are derived up to the quadratic bias parameter and are given by:

$$\delta b_{1,NG}^E(f_{\text{NL}}) = -\frac{1}{\delta_c} \frac{\nu}{R_{NG}} \frac{\partial R_{NG}}{\partial \nu}, \quad (2.13)$$

$$\delta b_{2,NG}^E(f_{\text{NL}}) = \frac{\nu^2}{\delta_c^2 R_{NG}} \frac{\partial^2 R_{NG}}{\partial \nu^2} + 2\nu(b_1^E - \frac{17}{21}) \delta b_{1,NG}^E, \quad (2.14)$$

where R_{NG} is the non-Gaussian correction to the mass function, as derived in Ref. [79], while its amplitude is regulated by f_{NL} (see also Appendix C of Ref. [22] for the analytic results and derivation). These corrections are absorbed into b_1 and b_2 in all the expressions for brevity. Henceforth, we drop the superscript E from the bias parameters, since we consider the HI statistics at the time of observation.

2.3 HI bias

The results of the general bias expansion (Sec. 2.2) are independent of the type of dark matter tracer [62]. Therefore, the final ingredient in the determination of the two-point and three-point 21cm galaxy correlators is the prescription of how the neutral hydrogen populates the dark matter halos. In the spirit of the halo model [81–83], we can define the density of the neutral hydrogen, assuming that there is negligible contribution outside of the halos, as [84, 85]

$$\rho_{HI}(z) = \int n_h(M, z) M_{HI}(M, z) d \ln M. \quad (2.15)$$

where M_{HI} is the average neutral hydrogen mass contained inside a halo of mass M at redshift z . Hence, the abundance of neutral hydrogen will be, $\Omega_{HI}(z) = \rho_{HI}(z)/\rho_c^0$.

Generalising the results of Ref. [85], where they provide the linear bias of the HI in the framework of the halo model, we retrieve the higher-order HI bias coefficients. The HI bias parameters are then given by:

$$b_{HI}^i(z) = \frac{1}{\rho_{HI}(z)} \int_0^\infty n_h(M, z) b_i^h(M, z) M_{HI}(M, z) d \ln M, \quad (2.16)$$

The expressions for the local-in-matter bias parameters b_N ($N \geq 1$) are derived by using the T08 mass function [Eq. (A.4)] and the PBS argument [Eq. (A.3)], where the details of the derivation are presented in Appendix A. In the case of the linear halo bias (i.e. b_1^h) instead of using the PBS bias results [Eq. (A.9)], we will use the best fit expression presented in Ref. [86], which achieves a better agreement with numerical results, for both low and high masses (see also Ref. [87]). The analytic expressions for the higher-order halo bias (i.e. $b_{i>1}^h$) derived in Appendix A [Eqs. (A.10)-(A.12)] were tested against simulations in Ref. [87]. They show that the "PBS+T08" prediction for b_2^h [Eq. (A.10)] deviate from their numerical results, mainly for low masses, while it still does better than the standard expression derived from the PBS argument and the mass function of Ref. [88] (hereafter ST99). In the case of b_3^h and b_4^h , the PBS-derived results from the T08 mass function [Eqs. (A.11) and (A.12)] are in agreement with their measurements. In order to ensure the self-consistency of this work, as well as to be congruent with the HI bias prediction of Ref. [85], we will use the "PBS+T08" results for the higher-order halo biases¹ [i.e. Eqs. (A.10)-(A.12)].

Note that, in Ref. [87] fitting formulas for b_2 and b_3 , as a function of b_1 , are provided. Using those, instead of the "PBS+T08" predictions, in our Fisher analysis change's the forecasts on the amplitude of PNG by few percent (1 – 4% depending the survey). The main reason for this change is the difference in the values of the bias parameters predicted by the two schemes. After the marginalization of the free parameters, which include the HI bias coefficients, the resulting f_{NL} forecasts from the two different bias schemes will differ, due to correlations between f_{NL} and the bias parameters. However, the HOD recipe (described next) used here favours mass ranges, where both halo bias predictions (i.e. the fitting formulas of Ref. [87] and those derived in Eqs. (A.10) and (A.11)) are consistent with each other. This explains the small change observed on f_{NL} forecasts, although the two halo bias schemes have different predictions. Simply put, using either of the two schemes does not have a significant impact on our Fisher forecasts.

The final ingredient of the HI bias recipe is the relation for the neutral hydrogen mass M_{HI} . Here we use the fitting results of Ref. [85]:

$$M_{HI}(M, z) = C(z)(1 - Y_p) \frac{\Omega_b}{\Omega_m} e^{-M_{min}(z)/M} M^{\alpha(z)} \quad (2.17)$$

where $Y_p = 0.24$ is the Helium fraction, M_{min} represents the halo mass below which the HI abundance in halos is exponentially suppressed, α controls the efficiency of processes generating or destroying HI inside halos, and C is a normalization constant fixed by the value of $\Omega_{HI}(z)$. Note that, the HI bias parameters do not depend on the normalization of M_{HI} . The values for the free parameters are considered to be, $\alpha = 1$ and $M_{min} = 5 \cdot 10^9 M_{sun}/h$. The resulting Eulerian bias parameters [Eq. (2.16)] are plotted as a function of redshift in

¹The results for b_3 and b_4 , although they are not part of the bias expansion up to second order [Eq. (2.9)], are presented due to their involvement in the theoretical error treatment presented in Sec. 4

Fig. 3. Alternative expressions for the neutral hydrogen mass, originating from comparisons with numerical results, are also presented in Refs. [89, 90].

2.4 Power spectrum and bispectrum of HI in redshift space

In order to model the HI power spectrum and bispectrum in redshift space, we extend the SPT kernels (see Ref. [46] for a review) to incorporate the bias expansion, discussed in Sec. 2.2, as well as the redshift space distortions (RSD) [91–93], which are treated perturbatively [94, 95]. The finger-of-god (FOG) effect [96] is treated phenomenologically, by introducing an exponential damping factor D_{FOG} , which characterizes the suppression of clustering power due to non-linear velocities. The analysis here is confined within the perturbative regime, where the leading order description for the redshift space power spectrum and bispectrum offers a good agreement with numerical measurements [97–100]. In the presence of a general, non-local, PNG the linear power spectrum and tree-level bispectrum in redshift space is given by (e.g. see Ref [22] for details):

$$P_{HI}^s(\mathbf{k}, z) = T_b(z)^2 [D_{\text{FOG}}^P(\mathbf{k}, z) Z_1(\mathbf{k}, z)^2 P_m^L(k, z) + P_\varepsilon(z)] + P_N(\mathbf{k}, z), \quad (2.18)$$

$$B_{HI}^s(\mathbf{k}_1, \mathbf{k}_2, \mathbf{k}_3, z) = T_b(z)^3 \left\{ D_{\text{FOG}}^B(\mathbf{k}_1, \mathbf{k}_2, \mathbf{k}_3, z) \left[Z_1(\mathbf{k}_1, z) Z_1(\mathbf{k}_2, z) Z_1(\mathbf{k}_3, z) B_I(k_1, k_2, k_3, z) \right. \right. \\ \left. \left. + \left\{ 2Z_1(\mathbf{k}_1, z) Z_1(\mathbf{k}_2, z) Z_2(\mathbf{k}_1, \mathbf{k}_2, z) P_m^L(k_1, z) P_m^L(k_2, z) + 2 \text{ perm} \right\} \right] \right. \\ \left. + 2P_{\varepsilon\varepsilon\delta}(z) \left[Z_1(\mathbf{k}_1, z) P_m^L(k_1, z) + 2 \text{ perm} \right] + B_\varepsilon(z) \right\}. \quad (2.19)$$

where P_N is the instrument noise (see Sec. 3) and T_b is the temperature function of the HI field. The expressions for the redshift space kernels [i.e. $Z_1(\mathbf{k})$ and $Z_2(\mathbf{k}_i, \mathbf{k}_j)$], as well as the FOG dumping effect (i.e. D_{FOG}), can be found in Appendix C. The redshift-space kernels depend on the line-of-sight direction \hat{z} , which breaks the statistical isotropy for the power spectrum and bispectrum. This means that, there is an additional angle needed to characterize the redshift space power spectrum, given by $\mu = \cos \omega = \hat{\mathbf{k}} \cdot \hat{z}$. Moreover, the bispectrum is no longer characterized only by the triangle shape (i.e. the length of three wave vectors k_1 , k_2 and k_3), but two additional variables are introduced to describe the orientation of the triangular configuration with respect to \hat{z} . The angle parametrization of [101] is used here, where the polar angle is $\omega = \cos^{-1}(\hat{\mathbf{k}}_1 \cdot \hat{z})$ and the azimuthal angle is ϕ . Then $\mu_1 = \cos \omega = \hat{\mathbf{k}}_1 \cdot \hat{z}$, $\mu_2 = \mu_1 \cos \theta_{12} + \sqrt{1 - \mu_1^2} \sin \theta_{12} \sin \phi$ and $\mu_3 = -(k_1/k_3)\mu_1 - (k_2/k_3)\mu_2$, where $\cos \theta_{12} = \hat{\mathbf{k}}_1 \cdot \hat{\mathbf{k}}_2$. Thus the parametrization of the redshift space bispectrum will be $B_{HI}^s(\mathbf{k}_1, \mathbf{k}_2, \mathbf{k}_3, z) = B_{HI}^s(k_1, k_2, k_3, \mu_1, \phi, z)$.

The temperature function is given, in μK , by (see the Appendix of Ref. [102])

$$T_b = 180(1+z)^2/E(z) \times 4 \times 10^{-4}(1+z)^{0.6} \quad (2.20)$$

where $E(z) = \sqrt{\Omega_m(1+z)^3 + \Omega_k(1+z) + \Omega_\Lambda}$, for the standard dark-energy model (i.e. $w_0 = -1$, $w_\alpha = 0$). The terms, P_ε , $P_{\varepsilon\varepsilon\delta}$, B_ε are generated by the presence of stochastic bias and their fiducial values are taken to be those predicted by Poisson statistics and are given by [62, 103]:

$$P_\varepsilon \equiv P_{\text{SN}}; \quad P_{\varepsilon\varepsilon\delta} = \frac{b_1}{2n_{\text{eff}}}; \quad B_\varepsilon = \frac{1}{n_{\text{eff}}^2}, \quad (2.21)$$

where, in the HI halo model approach (Sec. 2.3), the shot noise term is given by [85]:

$$P_{\text{SN}}(z) = \frac{1}{\bar{n}_{\text{eff}}(z)} = \frac{1}{\rho_{\text{HI}}(z)} \int n_h(M, z) M_{\text{HI}}^2 d \ln M \quad (2.22)$$

The tree-level redshift space bispectrum [Eq. (2.19)] has additional terms, originating from the presence of PNG, of $\mathcal{O}(f_{\text{NL}}^2)$. The fiducial value considered here for the PNG amplitude is $f_{\text{NL}} = 0$, hence they do not contribute to the signal in a Fisher matrix forecast. Therefore, they will be neglected here in order to simplify our calculations. As mentioned in Sec. 2.2, the scale-dependent non-Gaussian correction $b_{\Psi} k^\alpha / M(k)$ in Eq. (C.1), should be removed from the analysis in the case of equilateral PNG, for both power spectrum and bispectrum, due to strong degeneracies between $f_{\text{NL}}^{\text{equil}}$ and other parameters on both large and small scales [73], in order to avoid numerical contributions to the PNG signal that would be inaccessible by a LSS survey. Note that, the exclusion of large scales, due to foreground contamination (see Sec. 3.1), allows us to safely neglect wide-angle and relativistic effects in the HI bispectrum. The full expression of the large-scale bispectrum, beyond any approximated treatments, is shown in Ref. [104].

3 Modeling the thermal noise of 21 cm surveys

The main difference between a galaxy survey and a line intensity mapping survey is that in the latter there is a noise component associated with the instrument itself. Such component, in most cases, dominates over the shot-noise term, which is instead the dominant noise term in traditional galaxy surveys. We model this instrumental noise component as a Gaussian noise given by [105, 106]

$$P_{\text{N}}(\mathbf{k}, z) = T_{\text{sys}}^2(z) \chi^2(z) \lambda(z) \frac{(1+z)}{H(z)} \left(\frac{\lambda^2(z)}{A_e} \right)^2 \frac{1}{N_{\text{pol}} n_b(u) t_{\text{survey}}} \frac{S_{\text{area}}}{\theta_{\text{FOV}}^2} \quad (3.1)$$

for a radio interferometer. Here $T_{\text{sys}} = T_{\text{sky}} + T_{\text{inst}}$ is the system temperature, which is given from the sum between the sky and the instrument temperature (see Eq. D1 and D2 of [102]), and $\lambda(z)$ is the redshifted wavelength of the 21cm HI line. The field-of-view is θ_{FOV} and S_{area} is the area of the survey in steradians, while $n_b(u)$ is the antenna distribution (Appendix B), $N_{\text{pol}} = 2$ is the number of polarizations per feed and A_e is the effective beam area. Finally, χ and t_{survey} , are the co-moving distance and the total observation time in hours, respectively.

We consider three 21 cm IM surveys: CHIME [107], HIRAX [108] and the PUMA survey [23, 102]. CHIME is operating as we speak, while HIRAX is in advanced proposal stage. The PUMA represents a much more aggressive concept about what will be possible in the future with a larger investment in this field.

All these instruments are modeled somewhat simplistically. We consider realistic noise curves associated with a given distribution of baseline lengths, sky coverage and attainable system performance, but we skim over issues associated with realistic aperture synthesis due to earth rotation and angle of observation. We initially also assume a perfect phase calibration, but we will later on consider the impact of discarding the data inside the foreground wedge, to illustrate the importance of phase calibration. In short, the main goal of this paper is to investigate the scientific potential of these experiments to motivate the research into a complete control of systematics.

For the surveys PUMA and HIRAX, the field-of-view is $\theta_{\text{FOV}} = \lambda(z)/D_{\text{eff}}$ and the collecting area per feed is $A_e = \pi(D_{\text{eff}}/2)^2$. We assume an effective dish area, D_{eff} , due to the

<i>Parameters</i>	<i>CHIME</i>	<i>HIRAX</i>	PUMA(Full/Petite)
redshift	0.75 – 2.5	0.75 – 2	2 – 6
packing	packed cylinder array	square	hexagonal (50% fill)
N_{dish}	4×256	1,024	32,000/5,000
D_{dish}	$W_{cyl} = 20 \text{ m}, L_{cyl} = 100 \text{ m}$	6 m	6 m
f_{sky}	0.6	0.36	0.5
t_{tot}	10000 hrs	10000 hrs	40000 hrs
T_{inst}	50 K	50 K	50 K

Table 1. The basic specifications for three IM surveys considered here. For PUMA, the array is hexagonally close-packed

non-uniform illumination of the primary, given by $D_{\text{eff}}^2 = \eta_a D_{\text{dish}}^2$, where D_{dish} is the physical dish size and $\eta_a = 0.7$ is the aperture efficiency factor, taken to have the same value for both surveys (see Appendix D of [102] for a discussion). HIRAX is assumed to be square closed packed, while PUMA is hexagonally close packed with 50% fill factor (i.e. a random 50% of hexagonally closed packed lattice sites are empty, so the array is equivalent in size to that of twice the number of elements but with quarter baseline density). For baseline density we follow the fitting formulas of [102].

In the case of CHIME, which is a cylindrical interferometer, we define the field-of-view as, $\theta_{\text{FOV}} = (1.22\lambda(z)/W_{\text{cyl}})\pi/2$, where W_{cyl} is the width of the cylinder in meters. While, the effective beam is given by, $A_e = \eta L_{\text{cyl}} W_{\text{cyl}} N_{\text{cyl}}/N_{\text{dish}}$, where the optical efficiency is taken to be $\eta = 1$. In the case of the cylindrical interferometer, N_{dish} corresponds to the total number of feeds on $N_{\text{cyl}} = 4$ cylinders, while L_{cyl} is each cylinders length in meters. For the baseline distribution we take approximate analytical expression given in Appendix B.

We take the total observation time to be 10,000 hours for CHIME and HIRAX [109], following their published plans. For PUMA, we have a 50% filled array that will observe for 40,000 hours, which corresponds to 5 years.

The covered area for PUMA is half the sky, while for CHIME and HIRAX is 60% and 36% respectively. The specific values of the parameters needed to calculate the power spectrum noise are given in Table 1.

3.1 Foreground exclusions

Foregrounds are orders of magnitude brighter than the signal in 21 cm studies [110–113] and thus present an irreducible systematic. This effect makes the very small radial wavenumbers $k_{\parallel} = k\mu$ inaccessible [114, 115]. However, based on our understanding of the production mechanism of the radio foregrounds, mainly composed by free-free and synchrotron emission from our galaxy and other unresolved sources, we have very good reasons to believe that they are spectrally smooth. This characteristic allows us to distinguish them from the cosmological signal, up to some value of k_{\parallel} , without significant losses [110, 111, 116, 117]. The exact value, below which the recovery is impossible, is unknown and a range of opinions has been proposed in the literature (see e.g. Refs. [110–112, 116, 117]). For example, in Ref. [111] it is shown that a foreground cleaning can be achieved, making inaccessible only the modes that satisfy $k_{\parallel} < 0.02 \text{ h/Mpc}$.

On the other hand, reconstruction techniques, and in particular the forward model reconstruction framework [118–124], has been used for IM in order to retrieve the long wavelength modes lost to the foregrounds [125–127], increasing significantly the range of scales acces-

sible to a HI IM experiment. In particular, in Ref. [127] they manage to recover, almost perfectly, modes down to $k \simeq 0.01 h/\text{Mpc}$. In this work, we avoid completely the foreground contaminated region by throwing away all the modes with $k_{\parallel} < k_{\parallel,\text{min}}$. Following the findings of Refs. [125, 127] and the suggestion of Ref. [102], we choose an optimistic case, $k_{\parallel,\text{min}} = 0.01 h/\text{Mpc}$, and a pessimistic one, where we study the effect of increasing $k_{\parallel,\text{min}}$ to $0.05 h/\text{Mpc}$.

In practice, there is an additional instrumental effect named foreground wedge [128, 129]. Wedge arises because a single interferometric baseline will see a monochromatic source away from zenith, fringing along frequency direction in exactly the same manner as non-monochromatic source at zenith. A full array with sufficiently dense coverage of the $u - v$ plane can break this degeneracy, but only if phase calibration is sufficiently accurate and stable. To date, this has not been achieved in current generation of intensity mapping and epoch of reionization arrays. Nevertheless, it is important to stress that the foreground wedge is not a fundamental astrophysical limitation, but a technical issue.

We model the wedge by removing all modes that satisfy $k_{\parallel} < k_{\text{wedge}} k_{\perp}$. The aggressiveness of the cut k_{wedge} is determined by the source furthest from the zenith that can corrupt the data. The most conservative assumption is that of horizon wedge, where any monochromatic source above horizon can contaminate the data. 21 cm intensity mapping is not really competitive in this limit and therefore we do not consider this option. A more realistic modeling assumes that sources up to a certain number N_w of primary beam sizes away from the zenith can have an effect, giving [128]

$$k_{\text{wedge}} = \frac{rH(z)}{c(1+z)} \sin\left(1.22N_w \frac{\theta_{\text{FOV}}}{2}\right), \quad (3.2)$$

In this paper we consider values of $N_w = 0, 1, 3$, where $N_w = 0$ is the most optimistic (fully recovery of data inside the wedge) and $N_w = 3$ is the most pessimistic.

4 Fisher Matrix Analysis

The Fisher matrix formalism is utilised here to predict the uncertainty on the amplitude of primordial non-Gaussianity from HI IM surveys. The approach relies on the estimation of the likelihood distribution around its maximum, which is assumed to be a multivariate Gaussian, by Taylor expanding it up to second order. The Fisher information matrix is then given by the second derivative of the log-likelihood \mathcal{L} with respect to the parameters \mathbf{p} of the assumed model by:

$$F_{\alpha\beta} = - \left\langle \frac{\partial^2 \ln \mathcal{L}}{\partial p_{\alpha} \partial p_{\beta}} \right\rangle, \quad (4.1)$$

where \mathbf{p} is the parameter vector and α, β are the indices of the vector that correspond to the unknown parameters of interest. The inverse of the Fisher matrix $(F^{-1})_{\alpha\beta}$ yields an estimate of the parameter covariance, with the smallest possible uncertainty on the measurement errors (i.e. the Cramer-Rao bound). If all the free parameters of the model are measured simultaneously, we can derive the marginalised error on the parameter p_{α} , i.e. taking into account degeneracies and cross-correlations between the parameters on the final constrains, by $\sigma(p_{\alpha}) = \sqrt{(F^{-1})_{\alpha\alpha}}$.

In the case of the HI power spectrum, the Fisher matrix is given by

$$F_{\alpha\beta}^{Ps}(z) = \sum_k \int_{-1}^1 \frac{d\mu}{2} \frac{\partial P_{HI}^s(\mathbf{k}, z)}{\partial p_\alpha} \frac{\partial P_{HI}^s(\mathbf{k}, z)}{\partial p_\beta} \frac{1}{\Delta P^2(\mathbf{k}, z)}, \quad (4.2)$$

while for the bispectrum we have [130]

$$F_{\alpha\beta}^{Bs}(z) = \frac{1}{4\pi} \sum_T \int_{-1}^1 d\mu_1 \int_0^{2\pi} d\phi \frac{\partial B_{HI}^s(\mathbf{k}_1, \mathbf{k}_2, \mathbf{k}_3, z)}{\partial p_\alpha} \frac{\partial B_{HI}^s(\mathbf{k}_1, \mathbf{k}_2, \mathbf{k}_3, z)}{\partial p_\beta} \frac{1}{\Delta B^2(\mathbf{k}_1, \mathbf{k}_2, \mathbf{k}_3, z)}, \quad (4.3)$$

where the derivatives, for both correlators, are evaluated at the fiducial value of the parameter vector \mathbf{p} [Eq. (4.7)]. The sum over the triangles is denoted as Σ_T , where after applying the triangle condition, we take into consideration the symmetry under all permutations of \mathbf{k}_1 , \mathbf{k}_2 and \mathbf{k}_3 by restricting the summation of the magnitudes to $k_{\min} \leq k_3 \leq k_2 \leq k_1 \leq k_{\max}$. The bin size of the wavenumber magnitude is Δk , which is taken to be the fundamental frequency of the corresponding survey, $k_f = 2\pi/L$, where we approximate for simplicity the survey volume as a cube, $L = V^{1/3}$. This bin size is used, not only for the triangle summation in Eq. (4.3), but also for the wavenumber sum in Eq. (4.2). The wavenumber is binned between a minimum value $k_{\min} = k_f$, which is the largest scale available to each survey, and a maximum value k_{\max} , which corresponds to the smallest scale assumed.

In our Fisher matrix analysis, only the diagonal part of the covariance matrix (i.e. ΔP^2 and ΔB^2) is taken into consideration, neglecting all the cross-correlations between different triangles (bispectrum) and k -bins (power spectrum). We adopt a Gaussian approximation for the variance terms [131, 132]:

$$\Delta P^2(\mathbf{k}, z) = \frac{4\pi^2}{V_{\text{survey}}(z)k^2\Delta k(z)} P_{HI}^s(\mathbf{k}, z)^2, \quad (4.4)$$

$$\Delta B^2(\mathbf{k}_1, \mathbf{k}_2, \mathbf{k}_3, z) = s_{123}\pi V_f(z) \frac{P_{HI}^s(\mathbf{k}_1, z)P_{HI}^s(\mathbf{k}_2, z)P_{HI}^s(\mathbf{k}_3, z)}{k_1k_2k_3\Delta k(z)^3}, \quad (4.5)$$

where $s_{123} = 6, 2, 1$ for equilateral, isosceles and scalene triangles respectively. The volume of the fundamental shell in Fourier space is $V_f = k_f^3$. Higher order correlators are involved in the calculations of the off-diagonal terms of the covariance, for both the power spectrum (4-point) and the bispectrum (6-point) [131], which makes their implementation into the Fisher analysis very challenging. In Ref. [133] they study the halo power spectrum and bispectrum covariances by comparing to N-body simulations. In the case of the power spectrum, they demonstrate that for dense samples and the redshift ranges, like those considered here, the off-diagonal terms of the covariance can be safely neglected. Furthermore, for the bispectrum, they show that the off-diagonal part can be important for low density samples and at low redshifts, while for scales $k \gtrsim 0.1 h/\text{Mpc}$ these elements significantly deviate the covariance from the Gaussian approximation. However, for the samples, redshift ranges and scales considered in this work, we do not expect the exclusion of the off-diagonal part of the covariance to have a significant impact to our final PNG forecasts. On the other hand, higher-order corrections to the bispectrum variance (i.e. the diagonal part of the covariance), could have a significant effect not only for cosmological parameters [133], but also for PNG constraints [22]. The full non-Gaussian contribution to the variance, for the large scales considered in this work, can

be well approximated by perturbative corrections to the power spectrum appearing in Eq. (4.5), obtaining [133]:

$$\Delta B_{\text{NL}}^2(\mathbf{k}_1, \mathbf{k}_2, \mathbf{k}_3, z) = \Delta B^2(\mathbf{k}_1, \mathbf{k}_2, \mathbf{k}_3, z) + s_{123}\pi V_f(z) \frac{P_{HI}^s(\mathbf{k}_1, z)P_{HI}^s(\mathbf{k}_2, z)P_{HI}^{\text{NL}}(\mathbf{k}_3, z) + 2 \text{ perm}}{k_1 k_2 k_3 \Delta k(z)^3}, \quad (4.6)$$

where $P_{HI}^{\text{NL}}(\mathbf{k}, z)$ is given by Eq. (2.18) after substituting the linear power spectrum with the nonlinear correction, i.e. $P_m^L(k) \rightarrow P_{HI}^{\text{NL}}(k) - P_m^L(k)$, where the nonlinear power spectrum P_{NL}^{NL} is taken to be the HALOFIT power spectrum [134, 135]. For the bispectrum Fisher matrix forecasts [Eq. (4.3)], the variance with the non-Gaussian correction [Eq. (4.6)] will be used.

The set of free parameters that consist the parameter vector, used in the derivatives of the Fisher matrix formalism, is considered to be

$$\mathbf{p} = \{f_{\text{NL}}, b_1, b_2, b_{s^2}, P_\varepsilon, P_{\varepsilon\varepsilon\delta}, B_\varepsilon, f, \sigma_v\}. \quad (4.7)$$

where σ_v controls the strength of the FOG dumping factor (see Appendix C for the details). The stochastic bias contributions (i.e. $P_\varepsilon, P_{\varepsilon\varepsilon\delta}$ and B_ε) are considered here as nuisance parameters and they are marginalised over to acquire the Fisher sub-matrix for the parameters of interest, i.e. $f_{\text{NL}}, b_1, b_2, b_{s^2}, f, \sigma_v$. After acquiring the sub-matrix we marginalise over the rest of the free parameters for each redshift slice (see e.g. [136] for details on the process). Here the redshift slices are considered non-overlapping (i.e. cross-redshift correlation are considered to be zero). We then proceed to the summation of the final $F_{f_{\text{NL}}f_{\text{NL}}}(z)$ over the whole redshift range of each survey, in order to derive the final forecasts on the amplitude of PNG from each respective correlator, i.e. $F_{\alpha\beta}^{Ps}$ and $F_{\alpha\beta}^{Bs}$. We also consider the forecasts from the combined power spectrum and bispectrum Fisher matrices, i.e. $F_{\alpha\beta}^{Ps+B_s} = F_{\alpha\beta}^{Ps} + F_{\alpha\beta}^{Bs}$, where we neglect the cross-covariance between the two. This would have minimal impact on our forecasts [133]. Note that, cosmological parameters are considered to be known (fixed), since they can be measured with high accuracy by other probes (e.g. CMB, BAO etc.). For the CMB primordial bispectrum, it was shown in Ref. [137] that the degeneracies between cosmological parameters and f_{NL} are small, therefore we do not expect that the propagation for the cosmological errors will significantly impact the f_{NL} constraints. This was also pointed out, for the case of the galaxy power spectrum and bispectrum, in Refs. [78, 138, 139].

The Fisher analysis is confined inside the perturbative regime, where the SPT description of the power spectrum and bispectrum is reliable (for the latter see e.g. Refs. [97–100, 140]), by cutting the smallest scales at $k_{\text{max}} = 0.75k_{\text{NL}}(z)$. The non-linear scales k_{NL} are taken to be the linear, one dimensional velocity dispersion, given by

$$k_{\text{NL}}(z) = \left[\frac{1}{6\pi^2} \int_0^\infty dk P_{\text{lin}}(k, z) \right]^{-1/2}. \quad (4.8)$$

The increase of the maximum scales with redshift takes into advantage the fact that the Universe is more linear at higher redshifts, hence the tree-level description of the bispectrum holds up to higher values of k_{max} . This means that we can include more modes into the analysis for an increasing redshift, which will enhance the number of formed triangles and therefore the bispectrum signal (i.e. the information of the Fisher matrix) through the reduction of the cosmic variance.

Nonetheless, ignoring higher-to-leading order terms (i.e. 1-loop) in the modelling can affect the forecasts. In a perturbative approach each order has a limited range of validity and the higher order contributions could become important, while approaching the nonlinear regime. Although the analysis is limited up to linear scales and therefore the higher order corrections are not expected to significantly affect our forecasts, we take into account the parameter shift due to neglecting the 1-loop contributions at the level of the Fisher matrix, through the theoretical errors approach [141]. In this formalism the theoretical errors are defined as the difference between the chosen perturbative order (i.e. tree-level) and the next higher order (i.e. 1-loop). An envelope \mathbf{E} is fitted, bounding these errors, as a function of the wavenumber. Together with a correlation coefficient ρ_{ij} , which is assumed to be a multivariate Gaussian, we form a theoretical error covariance $C_{ij}^e = E_i \rho_{ij} E_j$, where i, j are the indices of the different momentum configurations (i.e. number of bins and triangles for the power spectrum and bispectrum respectively). The correlation coefficient takes into account the correlations between the different momentum configurations, making the impact of the theoretical errors independent of the k binning and the correlation length (see Ref. [141] for an extensive discussion). The final covariance used in the Fisher matrix analysis [Eqs. (4.2) and (4.3)] will be the sum of the error covariance C^e with the respective variance [i.e. Eqs. (4.4) and (4.6)]. The envelopes, for the power spectrum and bispectrum modelling, are taken from Ref. [22], where they have extended the approach of Ref. [141] to include the theoretical uncertainties from excluding the 1-loop terms of the matter and the local-in-matter bias expansions (i.e. b_1, b_2, b_3 , etc.) in the power spectrum and bispectrum, while performing an extensive study on the impact of theoretical errors on various parameters, including f_{NL} .

Note that the smallest accessible scales are also limited by the specifications of each survey. The largest and smallest available perpendicular scales are given by $k_{\perp, \text{min}} = 2\pi/(\chi\theta_{\text{FOV}})$ and $k_{\perp, \text{max}} = 2\pi D_{\text{max}}/(\lambda\chi)$ respectively. These limits originate from the intrinsic limitations of interferometers, which are fundamentally unable to probe any scale larger than those that correspond to their dish diameter [142]. All these scale limits, i.e. the foreground cut off ($k_{\parallel, \text{min}}$), the wedge [Eq. (3.2)], the intrinsic cut offs of the interferometer and the scale of model validity (k_{max}), constitute an observational window, where the signal of the HI power spectrum and bispectrum, in the redshift range considered, is non-zero. The signal from this window accounts for the forecast results presented in the next section. Note, that the window becomes more narrow as we go to higher redshifts, due to the increasing contamination, which for the case of the HI bispectrum leads to a significant reduction in the signal (see Fig. 1). For redshifts of the Epoch of Reionization, the window for the bispectrum could close completely and an aggressive foreground cleaning formalism would be needed [143].

5 Results

Our main results are summarized in Table 2. We give results for all three types of non-Gaussianity and for a number of wedge cuts. For comparison, the currently achieved sensitivities from Planck [144] are 5, 43 and 21 for squeezed, equilateral and orthogonal shapes respectively. Forecasted numbers for CMB-S4 experiments are 2, 21 and 9. SphereX can achieve 0.5 for the local shape. Galaxy surveys are generally unable to achieve competitive constraints for shapes which peak away from the squeezed limit, due to heavy contamination from non-linear gravitational effects; this is particularly true for the equilateral case, where late-time non-linear contributions are largest.

Wedge type	CHIME			HIRAX			PUMA Full (Petite)		
	NO	PB	3× PB	NO	PB	3× PB	NO	PB	3× PB
P(loc)	31.7	31.7	31.9	25.3	25.3	25.8	1.61 (1.67)	1.72 (1.77)	2.52 (2.57)
B(loc)	71.9	71.9	72.7	9.2	9.2	10.2	0.31 (0.77)	0.41 (0.91)	0.91 (1.67)
P+B(loc)	28.2	28.2	28.4	8.4	8.5	9.3	0.3 (0.69)	0.4 (0.8)	0.84 (1.37)
P(equil)	-	-	-	-	-	-	-	-	-
B(equil)	569.9	569.9	576.7	98.0	98.3	112.5	11.66 (21.87)	16.71 (27.09)	41.99 (55.49)
P+B(equil)	257.3	257.3	259.8	51.7	51.9	59.1	5.06 (10.15)	7.98 (13.29)	23.17 (29.38)
P(ortho)	937.9	937.9	940.3	613.6	613.6	662.4	39.41 (45.29)	46.94 (51.71)	74.97 (78.96)
B(ortho)	215.3	215.3	216.7	34.9	35.0	38.4	3.13 (7.33)	4.22 (8.52)	8.86 (14.28)
P+B(ortho)	158.2	158.2	159.5	28.5	28.5	31.8	3.04 (6.53)	4.08 (7.79)	8.56 (13.32)

Table 2. Forecasts for the $1 - \sigma$ error of the primordial non-Gaussian amplitude in the case of the three PNG types considered here. These results come from the summation of the signal over the whole redshift range of each survey, where we show the constraints originating from the galaxy power spectrum, bispectrum and their combined signal. In addition, different wedge cases are considered for each survey. The forecasts under the column "NO" correspond to the case where no wedge cut is used, while under the columns titled "PB" and "3xPB" are the forecasts after applying the prime-beam wedge cuts [Eq. (3.2)] for $N_w = 1$ and $N_w = 3$ respectively. Moreover, we exclude from the analysis all scales that satisfy, $k_{\parallel} < 0.01$ h/Mpc, as discussed in the main text. The forecasts under "3xPB" correspond to the main results of this work.

We see that CHIME is never competitive, despite significant volume coverage, because the thermal noise is overwhelming. HIRAX could instead achieve similar sensitivities to Planck. These constraints will be independent and could therefore improve over Planck by some 40%. Most importantly, if such result will be achievable in practice – keeping all systematics under control – it will provide an outstanding observational confirmation that primordial non-Gaussianity is indeed a very promising field of study for future, ambitious intensity mapping surveys. Our forecasts show that PUMA should be competitive with CMB-S4 and Spherex. Notably, it could provide particularly strong constraints for the equilateral shape, if the foreground wedge could be controlled. This is of particular interest, considering the general difficulty of improving equilateral constraints using LSS tracers, as mentioned above.

In Fig. 1 we study where the information is coming from, as a function of redshift. In general, the neutral hydrogen maps are noisier at higher redshift, due to increasing sky noise temperature and decreasing bandwidth per comoving distance. This is partly offset by the fact that the non-linear scale is smaller at higher redshift (i.e. increasing $k_{NL}(z)$), and that the total volume per sky area is larger. As a result, there are no unique trends and different experiments can extract most information from either low or high redshift end, depending both on the experiment and on the type of non-Gaussianity under consideration.

In most cases, presented in Fig. 1, the majority of the PNG signal originates from the bispectrum (see also Table 2), highlighting the importance of three-point statistics in constraining PNG from future IM experiments, and in particular from packed interferometric arrays. At higher redshift slices the Universe becomes more linear, increasing the scale range where the linear theory is still valid (increasing k_{\max}). A boost in the constraining power of the bispectrum is hence expected, due to the growing number of formed triangles and the amplitude reduction of the gravitational contaminants. This can be observed in some cases shown in Fig. 1, but a trend cannot be established due to the presence of observational and other effects (see Sec. 3.1), as well as due to the individual traits of the PNG types considered.

In the case of local PNG, the bispectrum signal peaks on the squeezed configurations

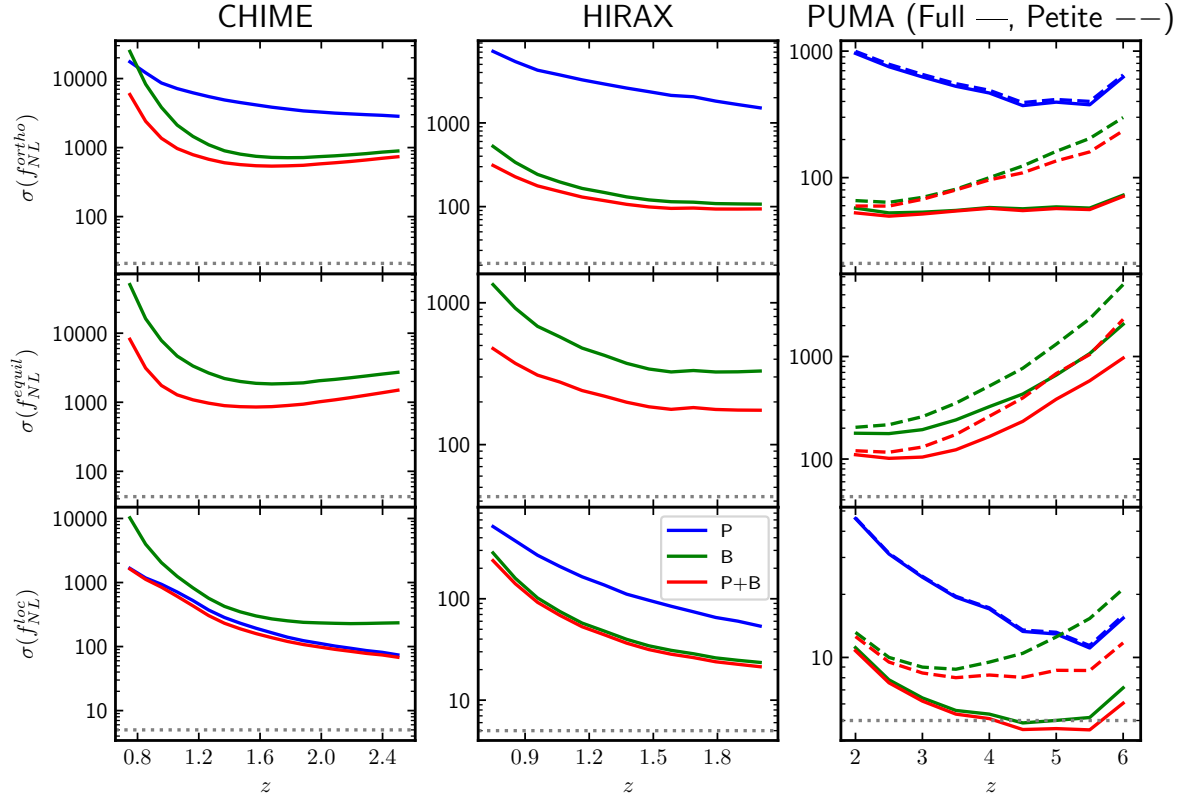


Figure 1. The forecasts for the non-Gaussian amplitude, in the case of the three types of PNG considered here, after marginalising over the free parameters. The results from the powerspectrum (blue), bispectrum (green) and their combined signal (red) are plotted as a function of redshift, while each column corresponds to one of the three surveys considered in this work. Each point of the lines corresponds to a fixed redshift slice with $dz = 0.1$. The "3 \times prime-beam" wedge is used, as well as we exclude all scales that satisfy, $k_{\parallel} < 0.01$ h/Mpc. The dotted grey line indicates the best constraints on the PNG amplitude, as given by Ref. [144].

($k_1 \ll k_2 \sim k_3$), therefore sufficiently large and small (up to the validity of linear theory) scales must be accessible by a survey, in order to have enough squeezed triangles to produce compelling bispectrum constraints. If they are restricted, due to e.g. observational and instrumental effects or low redshift slices (i.e. smaller linear regime), then the scale-dependence in the galaxy power spectrum provides most of the PNG signal. This is the case for CHIME and PUMA Petite, where for the latter this is evident for the large redshift slices (i.e. $z \geq 5$).

In the equilateral PNG scenario, the scale-dependent bias term approaches a constant value on large scales. In addition, as was discussed before, the presence of degeneracies between $f_{\text{NL}}^{\text{equil}}$ and other parameters [73], strip power spectrum from essentially any constraining power on equilateral PNG. This leaves galaxy bispectrum to be the sole contributor of the signal. The increasing range of the linear regime (i.e. increase in the number of the formed equilateral triangles) with redshift, in the cases of CHIME and HIRAX, improves the constraints on $f_{\text{NL}}^{\text{equil}}$, up to a saturation point due to the applied scale cuts (see Sec. 3.1 and Sec. 4). These scale limitations are the ones responsible for the opposite trend observed in the PUMA results. Due to the pessimistic wedge cuts, as well as the $k_{\text{min},\parallel}$ and k_{max} limits, the expected wide scale range, accessible to PUMA, is shrunken towards high redshift slices, ren-

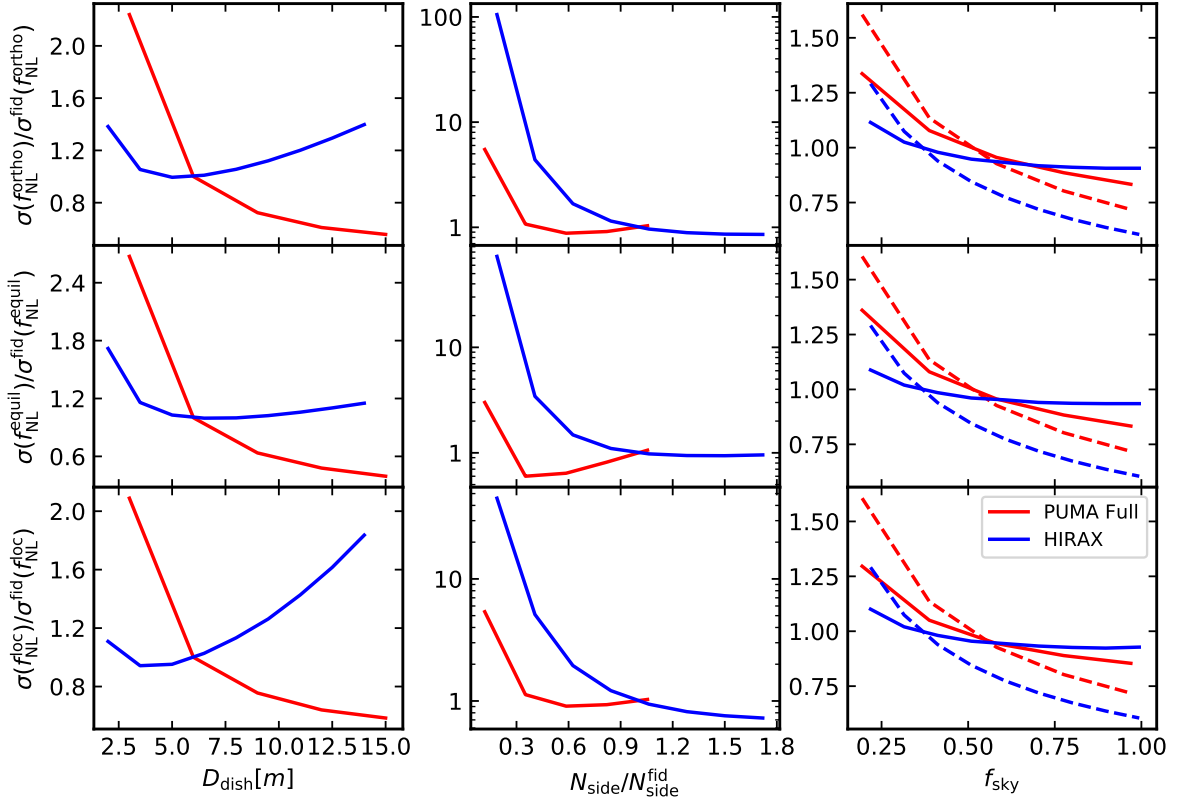


Figure 2. The PUMA (red) and HIRAX (blue) forecasts on f_{NL} , normalised over the fiducial forecasts (see Table 2), for the three PNG shapes considered here, as a function of the dish size (lefts panels), the number of dishes in each side (middle panels) and f_{sky} (right panels). All the remaining parameters (including integration time) are kept fixed for all three cases, beside the N_{side} case (middle panels), where in addition we keep fixed the collecting area. These results correspond to the combined power spectrum and bispectrum signal, after summing over the whole redshift range of the survey. The prime-beam wedge for $N_w = 3$ is used, as well as all scales that satisfy, $k_{\parallel} < 0.01$ h/Mpc, are excluded. The plotted dashed lines in the right panels represent the function, $(f_{\text{sky}}/f_{\text{sky}}^{\text{fid}})^{-1/2}$. Note that, in the middle panels the results for PUMA reach up to $N_{\text{side}}/N_{\text{side}}^{\text{fid}} \sim 1.1$ due to the tremendous increase in the calculation time. Nonetheless, the significant part of the functional dependence is shown.

dering their contribution to the integrated signal minimal. The same behaviour is observed for orthogonal PNG, where the effect of the k-cuts can be now seen also in the power spectrum constraints. Due to the functional form of the orthogonal PNG scale-dependent bias [69, 76], only the very high redshift slices of PUMA are affected by the scale cuts.

In Fig. 2 we show how experimental design parameters affect constraints for HIRAX and PUMA. We consider several changes. Changing the dish size (keeping other parameters fixed), moves sensitivity wholesale towards smaller perpendicular scales, affecting the minimum available k_{\perp} , but also raising the higher k_{\perp} available. The increase of the dish size decreases the thermal noise, due to the functional form of the baseline distribution² [Eq. (B.1)], while the value of the wedge cutoff k_{wedge} is also decreased due to the dependence on θ_{FOV} , allowing more modes to be used in the Fisher analysis. The latter is particularly

²Note that, this would not be the case, if a uniform baseline distribution had been used.

important for the PNG signal originating from the high redshifts, especially those accessible to PUMA, since the contaminated region is increased with redshift due to the dependence on the comoving distance and the Hubble parameter [Eq. (3.2)]. Therefore we find that PUMA prefers bigger dishes, while for HIRAX the 6m design size is nearly optimal (left panels in Fig. 2). Second, changing the number of dishes at fixed collecting area (middle panels in Fig. 2) lowers the noise power spectrum while keeping the resolution the same. We parametrize this with a parameter $N_{\text{side}} = \sqrt{N_{\text{dishes}}}$, which reduces to just the side of the array measured in the number of dishes for HIRAX. Naively, one would expect that increasing N_{side} can only improve the results, until the sample variance starts to dominate and the results converge to volume limited measurement. However, we find that this is not the case for PUMA, where increasing N_{side} actually makes things worse, especially for the equilateral case. This is because this exercise is done at the $N_{\text{w}} = 3$ wedge cut. Increasing the number of dishes at fixed collecting area makes dishes smaller, exacerbating the wedge cut. As a result, PUMA prefers larger dishes at fixed collecting area, which is consistent with our previous observation, i.e. after changing the dish size (left panels of Fig. 2). In the final column we plot trends with the observed sky area. This is done at a fixed observation time, so the smaller f_{sky} implies a smaller fraction of the sky, but observed with a lower noise level. We would therefore expect the error bars to follow

$$\sigma \propto \left(\frac{P_S + P_{\text{SN}} + \frac{f_{\text{sky}}}{f_{\text{sky, fid}}} P_N}{f_{\text{sky}}} \right)^{-1/2}. \quad (5.1)$$

In other words, for the sample variance limited case, we expect the sensitivity to improve as $f_{\text{sky}}^{-1/2}$ (plotted as dashed lines) and for the thermal noise dominated case we expect curves to flatten. We find that HIRAX indeed flattens out, but that PUMA is somewhere between the two limits.

Finally in Table 3 we study the effect of changing the irreducible value of foreground filtering $k_{\parallel, \text{min}}$. Since foregrounds affect mostly large angular scales, we find that the effect is the largest for the squeezed triangle configurations, which contain one small side. This leads to a significant decrease in the constraining power of both power spectrum and bispectrum in the local PNG case. The reduction is still very pronounced for orthogonal configurations. This is not completely intuitive, but explainable with the fact that the orthogonal shape presents a non-negligible correlation with the squeezed one, and takes significant contributions from flattened triangles. Equilateral PNG is the least affected, as expected, since only a small amount of equilateral triangles, formed by the largest scales, are excluded.

6 Conclusions

In this paper we have studied constraints on primordial non-Gaussianity from present and future 21 cm intensity mapping experiments. Since these experiments cover huge volumes of space, it is intuitive that they should be able to produce competitive non-Gaussianity results.

We find that a futuristic experiment such as PUMA will produce very competitive non-Gaussianity bounds from purely internal measurements of the power spectrum and bispectrum (see Table 2). This applies in particular to orthogonal and equilateral shapes, generally very hard to constrain using galaxy surveys, due to heavy contamination from non-linear late time evolution of structures. In the case of PUMA, this issue is offset by large volume coverage and nearly sample variance limited measurements. Moreover, at higher redshift, where the non-linear scale is smaller (larger k_{NL}), the increasing number of formed triangles leads to a

$k_{\parallel, \min}$ [h/Mpc]	CHIME		HIRAX		PUMA Full	
	0.01	0.05	0.01	0.05	0.01	0.05
P(loc)	31.9	105.5	25.8	101.3	2.52	8.42
B(loc)	72.7	457.7	10.2	71.5	0.91	3.63
P+B(loc)	28.4	101.7	9.3	47.9	0.84	3.05
P(equil)	-	-	-	-	-	-
B(equil)	576.7	3139.0	112.5	484.5	42	77.88
P+B(equil)	259.8	777.4	59.1	122.1	23.17	30.38
P(ortho)	940.3	1502.9	662.4	906.6	74.97	80.32
B(ortho)	216.7	1242.5	38.4	203.8	8.86	30.24
P+B(ortho)	159.5	600.5	31.8	102.3	8.56	24.25

Table 3. Same as in Table 2, but now we test the effect of the $k_{\parallel, \min}$ cuts on the f_{NL} forecasts. We fix the wedge cuts to be as in the case of "3× prime-beam" (i.e. $N_w = 3$ in Eq. (3.2)) and consider two values of the k_{\parallel} cut. Therefore the results that are under the " $k_{\parallel, \min} = 0.01$ " columns correspond to the main results of this work (i.e. same as "3×PB" of Table 2).

growth in the bispectrum signal. Additionally the amplitude reduction of the gravitational contaminants, leads to a promising PNG signal for high redshift surveys. In the case of PUMA, we find that the presence of foreground wedge significantly worsens the limits derived from the high redshift slices (see Fig. 1). It is therefore imperative that this important systematic is brought under control.

We find that constraints on the local shape of bispectrum are tight, but considerably less impressive compared to other probes of non-Gaussianity, such as those coming from LSST [22] or the upcoming SPHEREx experiment [145]. This is because the foreground cut at $k_{\parallel, \min} = 0.01h/\text{Mpc}$ leads to loss of information on large scale modes, which are required in the squeezed limit. While PUMA on its own is not competitive, cross-correlations between the small scale two-point function from PUMA and large scale mode measured by other means (traditional galaxy survey or CMB lensing) could yet prove to be very effective in measuring local non-Gaussianity (see Refs. [34, 35] for a multi-wavelength power spectrum application). We leave this work for the future.

We find that the current and upcoming generation of 21 cm surveys, such as CHIME and HIRAX are in general not very competitive. This boils down mainly to a considerable thermal noise in the field measurements. Any departure from sample variance limit hits the bispectrum measurement more than the power spectrum measurement and this leads to relatively non-competitive numbers in this case.

We also find that the difference between the full and petite versions of PUMA is pretty modest in the case of pessimistic foreground, but can be considerable if no wedge is assumed. The main difference between these two experiments is in angular resolution, as the full PUMA is simply an extended version of PUMA Petite. This leads to both, additional information on smaller scales but also improved sampling of large scales, since the number of short baselines increases too. What we see is a complex interplay between the change in noise and increase in the number of possible triangle configurations, that depend on both the maximum wavenumbers, but also any other cuts on the Fourier plane. The bottom line is that minimizing the effect of the foreground wedge is essential in order to extract all possible science from these measurements.

In traditional radio astronomy intuition, splitting the same collecting area into more interferometric elements always improves results, because it increases the field of view at constant noise. We find, however, that wedge considerations favor larger dishes, even at the same total collecting area. Since dishes can be thought of as analog interferometers, this in effect boils down to the relative difficulty of analog phase calibration (i.e. surface accuracies) vs electronic phase calibration. The actual trade off calculation will require more sophisticated studies of relative contributions of individual element repeatability and stability, interferometric phase control and data reduction software imperfections to the total error.

To conclude, measurements of primordial non-Gaussianity are ideally suited to intensity mapping of 21 cm neutral hydrogen across cosmic epochs, provided the thermal noise can be made smaller with a sufficiently large array and assuming systematics can be brought under control. Stage II 21 cm experiments such as PUMA will be therefore able to make impressive measurements of non-Gaussianity.

Acknowledgments:

The authors would like to thank Emanuele Castorina for useful comments on the draft of the manuscript, as well as Titouan Lazeyras for helpful feedback on the first arXiv version. ML's work is supported by the University of Padova under the STARS Grants programme CoG-ITO, Cosmology beyond Gaussianity, Inference, Theory and Observations. ML acknowledges support from the INDARK INFN Initiative (web.infn.it/CSN4/IS/Linea5/InDark).

References

- [1] P. D. Meeburg, D. Green, R. Flauger, B. Wallisch, M. C. D. Marsh, E. Pajer et al., *Primordial Non-Gaussianity*, *BAAS* **51** (2019) 107 [[1903.04409](https://arxiv.org/abs/1903.04409)].
- [2] M. Alvarez, T. Baldauf, J. R. Bond, N. Dalal, R. de Putter, O. Doré et al., *Testing Inflation with Large Scale Structure: Connecting Hopes with Reality*, *arXiv e-prints* (2014) arXiv:1412.4671 [[1412.4671](https://arxiv.org/abs/1412.4671)].
- [3] N. Bartolo, S. Matarrese and A. Riotto, *Non-Gaussianity in the curvaton scenario*, *Phys. Rev. D* **69** (2004) 043503 [[arXiv:hep-ph/0309033](https://arxiv.org/abs/hep-ph/0309033)].
- [4] M. Sasaki, J. Väliviita and D. Wands, *Non-Gaussianity of the primordial perturbation in the curvaton model*, *Phys. Rev. D* **74** (2006) 103003 [[astro-ph/0607627](https://arxiv.org/abs/astro-ph/0607627)].
- [5] C. T. Byrnes, K.-Y. Choi and L. M. H. Hall, *Conditions for large non-Gaussianity in two-field slow-roll inflation*, *Journal of Cosmology and Astro-Particle Physics* **10** (2008) 8 [[0807.1101](https://arxiv.org/abs/0807.1101)].
- [6] C. T. Byrnes, K.-Y. Choi and L. M. H. Hall, *Large non-Gaussianity from two-component hybrid inflation*, *Journal of Cosmology and Astro-Particle Physics* **2** (2009) 17 [[0812.0807](https://arxiv.org/abs/0812.0807)].
- [7] C. T. Byrnes and G. Tasinato, *Non-Gaussianity beyond slow roll in multi-field inflation*, *Journal of Cosmology and Astro-Particle Physics* **8** (2009) 16 [[0906.0767](https://arxiv.org/abs/0906.0767)].
- [8] C. T. Byrnes and K.-Y. Choi, *Review of Local Non-Gaussianity from Multifield Inflation*, *Advances in Astronomy* **2010** (2010) [[1002.3110](https://arxiv.org/abs/1002.3110)].
- [9] A. Linde and V. Mukhanov, *Non-Gaussian isocurvature perturbations from inflation*, *Phys. Rev. D* **56** (1997) R535 [[astro-ph/9610219](https://arxiv.org/abs/astro-ph/9610219)].
- [10] M. Zaldarriaga, *Non-Gaussianities in models with a varying inflaton decay rate*, *Phys. Rev. D* **69** (2004) 043508 [[astro-ph/0306006](https://arxiv.org/abs/astro-ph/0306006)].

- [11] P. Creminelli, *On non-Gaussianities in single-field inflation*, *Journal of Cosmology and Astro-Particle Physics* **10** (2003) 003 [[astro-ph/0306122](#)].
- [12] D. Seery and J. E. Lidsey, *Primordial non-Gaussianities in single-field inflation*, *Journal of Cosmology and Astro-Particle Physics* **6** (2005) 003 [[astro-ph/0503692](#)].
- [13] N. Bartolo, E. Komatsu, S. Matarrese and A. Riotto, *Non-Gaussianity from inflation: theory and observations*, *Phys. Rep.* **402** (2004) 103 [[astro-ph/0406398](#)].
- [14] E. Komatsu, N. Afshordi, N. Bartolo, D. Baumann, J. R. Bond, E. I. Buchbinder et al., *Non-Gaussianity as a Probe of the Physics of the Primordial Universe and the Astrophysics of the Low Redshift Universe*, *astro2010: The Astronomy and Astrophysics Decadal Survey* **2010** (2009) 158 [[0902.4759](#)].
- [15] Planck Collaboration, Y. Akrami, F. Arroja, M. Ashdown, J. Aumont, C. Baccigalupi et al., *Planck 2018 results. IX. Constraints on primordial non-Gaussianity*, *arXiv e-prints* (2019) arXiv:1905.05697 [[1905.05697](#)].
- [16] A. Slosar, C. Hirata, U. Seljak, S. Ho and N. Padmanabhan, *Constraints on local primordial non-Gaussianity from large scale structure*, *Journal of Cosmology and Astro-Particle Physics* **2008** (2008) 031 [[0805.3580](#)].
- [17] A. J. Ross, W. J. Percival, A. Carnero, G.-b. Zhao, M. Manera, A. Raccañelli et al., *The clustering of galaxies in the SDSS-III DR9 Baryon Oscillation Spectroscopic Survey: constraints on primordial non-Gaussianity*, *MNRAS* **428** (2013) 1116 [[1208.1491](#)].
- [18] T. Giannantonio, A. J. Ross, W. J. Percival, R. Crittenden, D. Bacher, M. Kilbinger et al., *Improved primordial non-Gaussianity constraints from measurements of galaxy clustering and the integrated Sachs-Wolfe effect*, *Phys. Rev. D* **89** (2014) 023511 [[1303.1349](#)].
- [19] B. Leistedt, H. V. Peiris and N. Roth, *Constraints on Primordial Non-Gaussianity from 800 000 Photometric Quasars*, *Phys. Rev. Lett.* **113** (2014) 221301 [[1405.4315](#)].
- [20] D. Karagiannis, T. Shanks and N. P. Ross, *Search for primordial non-Gaussianity in the quasars of SDSS-III BOSS DR9*, *MNRAS* **441** (2014) 486 [[1310.6716](#)].
- [21] E. Castorina, N. Hand, U. Seljak, F. Beutler, C.-H. Chuang, C. Zhao et al., *Redshift-weighted constraints on primordial non-Gaussianity from the clustering of the eBOSS DR14 quasars in Fourier space*, *Journal of Cosmology and Astro-Particle Physics* **2019** (2019) 010 [[1904.08859](#)].
- [22] D. Karagiannis, A. Lazanu, M. Liguori, A. Raccañelli, N. Bartolo and L. Verde, *Constraining primordial non-Gaussianity with bispectrum and power spectrum from upcoming optical and radio surveys*, *MNRAS* **478** (2018) 1341 [[1801.09280](#)].
- [23] A. Slosar, Z. Ahmed, D. Alonso, M. A. Amin, E. J. Arena, K. Bandura et al., *Packed Ultra-wideband Mapping Array (PUMA): A Radio Telescope for Cosmology and Transients*, in *BAAS*, vol. 51, p. 53, Sep, 2019, [1907.12559](#).
- [24] SKA collaboration, D. J. Bacon et al., *Cosmology with Phase 1 of the Square Kilometre Array: Red Book 2018: Technical specifications and performance forecasts*, *Publ. Astron. Soc. Austral.* **37** (2020) e007 [[1811.02743](#)].
- [25] S. Camera, M. G. Santos and R. Maartens, *Probing primordial non-Gaussianity with SKA galaxy redshift surveys: a fully relativistic analysis*, *MNRAS* **448** (2015) 1035 [[1409.8286](#)].
- [26] S. Camera, M. G. Santos, P. G. Ferreira and L. Ferramacho, *Cosmology on Ultralarge Scales with Intensity Mapping of the Neutral Hydrogen 21 cm Emission: Limits on Primordial Non-Gaussianity*, *Physical Review Letters* **111** (2013) 171302 [[1305.6928](#)].
- [27] D. Alonso and P. G. Ferreira, *Constraining ultralarge-scale cosmology with multiple tracers in optical and radio surveys*, *Phys. Rev. D* **92** (2015) 063525 [[1507.03550](#)].

- [28] N. Dalal, O. Doré, D. Huterer and A. Shirokov, *Imprints of primordial non-Gaussianities on large-scale structure: Scale-dependent bias and abundance of virialized objects*, *Phys. Rev. D* **77** (2008) 123514 [0710.4560].
- [29] S. Matarrese and L. Verde, *The Effect of Primordial Non-Gaussianity on Halo Bias*, *ApJ* **677** (2008) L77 [0801.4826].
- [30] N. Afshordi and A. J. Tolley, *Primordial non-Gaussianity, statistics of collapsed objects, and the integrated Sachs-Wolfe effect*, *Phys. Rev. D* **78** (2008) 123507 [0806.1046].
- [31] L. Verde and S. Matarrese, *Detectability of the Effect of Inflationary Non-Gaussianity on Halo Bias*, *ApJ* **706** (2009) L91 [0909.3224].
- [32] M. Santos, P. Bull, D. Alonso, S. Camera, P. Ferreira, G. Bernardi et al., *Cosmology from a SKA HI intensity mapping survey*, in *Advancing Astrophysics with the Square Kilometre Array (AASKA14)*, p. 19, April, 2015, 1501.03989.
- [33] S. Cunnington, S. Camera and A. Poursidou, *The degeneracy between primordial non-Gaussianity and foregrounds in 21cm intensity mapping experiments*, 2007.12126.
- [34] J. Fonseca, S. Camera, M. G. Santos and R. Maartens, *Hunting Down Horizon-scale Effects with Multi-wavelength Surveys*, *ApJ* **812** (2015) L22 [1507.04605].
- [35] D. Alonso and P. G. Ferreira, *Constraining ultralarge-scale cosmology with multiple tracers in optical and radio surveys*, *Phys. Rev. D* **92** (2015) 063525 [1507.03550].
- [36] Y. Xu, X. Wang and X. Chen, *Forecasts on the Dark Energy and Primordial Non-Gaussianity Observations with the Tianlai Cylinder Array*, *ApJ* **798** (2015) 40 [1410.7794].
- [37] X. Chen, *The Tianlai Project: a 21CM Cosmology Experiment*, in *International Journal of Modern Physics Conference Series*, vol. 12 of *International Journal of Modern Physics Conference Series*, pp. 256–263, Mar., 2012, 1212.6278, DOI.
- [38] Planck Collaboration, P. A. R. Ade, N. Aghanim, M. Arnaud, M. Ashdown, J. Aumont et al., *Planck 2015 results. XIII. Cosmological parameters*, *A&A* **594** (2016) A13 [1502.01589].
- [39] A. Lewis, A. Challinor and A. Lasenby, *Efficient Computation of Cosmic Microwave Background Anisotropies in Closed Friedmann-Robertson-Walker Models*, *ApJ* **538** (2000) 473 [astro-ph/9911177].
- [40] D. S. Salopek and J. R. Bond, *Nonlinear evolution of long-wavelength metric fluctuations in inflationary models*, *Phys. Rev. D* **42** (1990) 3936.
- [41] A. Gangui, F. Lucchin, S. Matarrese and S. Mollerach, *The three-point correlation function of the cosmic microwave background in inflationary models*, *ApJ* **430** (1994) 447 [astro-ph/9312033].
- [42] L. Verde, L. Wang, A. F. Heavens and M. Kamionkowski, *Large-scale structure, the cosmic microwave background and primordial non-Gaussianity*, *MNRAS* **313** (2000) 141 [astro-ph/9906301].
- [43] E. Komatsu and D. N. Spergel, *Acoustic signatures in the primary microwave background bispectrum*, *Phys. Rev. D* **63** (2001) 063002 [astro-ph/0005036].
- [44] P. Creminelli, A. Nicolis, L. Senatore, M. Tegmark and M. Zaldarriaga, *Limits on non-Gaussianities from WMAP data*, *Journal of Cosmology and Astro-Particle Physics* **5** (2006) 004 [astro-ph/0509029].
- [45] L. Senatore, K. M. Smith and M. Zaldarriaga, *Non-Gaussianities in single field inflation and their optimal limits from the WMAP 5-year data*, *Journal of Cosmology and Astro-Particle Physics* **1** (2010) 028 [0905.3746].
- [46] F. Bernardeau, S. Colombi, E. Gaztañaga and R. Scoccimarro, *Large-scale structure of the Universe and cosmological perturbation theory*, *Phys. Rep.* **367** (2002) 1 [astro-ph/0112551].

- [47] P. Coles, *Galaxy formation with a local bias*, *MNRAS* **262** (1993) 1065.
- [48] J. N. Fry and E. Gaztanaga, *Biasing and hierarchical statistics in large-scale structure*, *ApJ* **413** (1993) 447 [[astro-ph/9302009](#)].
- [49] J. N. Fry, *The Evolution of Bias*, *ApJ* **461** (1996) L65.
- [50] P. Catelan, F. Lucchin, S. Matarrese and C. Porciani, *The bias field of dark matter haloes*, *MNRAS* **297** (1998) 692 [[astro-ph/9708067](#)].
- [51] P. Catelan, C. Porciani and M. Kamionkowski, *Two ways of biasing galaxy formation*, *MNRAS* **318** (2000) L39 [[astro-ph/0005544](#)].
- [52] P. McDonald and A. Roy, *Clustering of dark matter tracers: generalizing bias for the coming era of precision LSS*, *Journal of Cosmology and Astro-Particle Physics* **8** (2009) 020 [[0902.0991](#)].
- [53] A. Elia, S. Kulkarni, C. Porciani, M. Pietroni and S. Matarrese, *Modelling the clustering of dark matter haloes in resummed perturbation theories*, *MNRAS* **416** (2011) 1703 [[1012.4833](#)].
- [54] K. C. Chan, R. Scoccimarro and R. K. Sheth, *Gravity and large-scale nonlocal bias*, *Phys. Rev. D* **85** (2012) 083509 [[1201.3614](#)].
- [55] T. Baldauf, U. Seljak, V. Desjacques and P. McDonald, *Evidence for quadratic tidal tensor bias from the halo bispectrum*, *Phys. Rev. D* **86** (2012) 083540 [[1201.4827](#)].
- [56] V. Assassi, D. Baumann, D. Green and M. Zaldarriaga, *Renormalized halo bias*, *Journal of Cosmology and Astro-Particle Physics* **8** (2014) 056 [[1402.5916](#)].
- [57] L. Senatore, *Bias in the effective field theory of large scale structures*, *Journal of Cosmology and Astro-Particle Physics* **11** (2015) 007 [[1406.7843](#)].
- [58] M. Mirbabayi, F. Schmidt and M. Zaldarriaga, *Biased tracers and time evolution*, *Journal of Cosmology and Astro-Particle Physics* **7** (2015) 030 [[1412.5169](#)].
- [59] A. Dekel and O. Lahav, *Stochastic Nonlinear Galaxy Biasing*, *ApJ* **520** (1999) 24 [[astro-ph/9806193](#)].
- [60] A. Taruya and J. Soda, *Stochastic Biasing and the Galaxy-Mass Density Relation in the Weakly Nonlinear Regime*, *ApJ* **522** (1999) 46 [[astro-ph/9809204](#)].
- [61] T. Matsubara, *Stochasticity of Bias and Nonlocality of Galaxy Formation: Linear Scales*, *ApJ* **525** (1999) 543 [[astro-ph/9906029](#)].
- [62] V. Desjacques, D. Jeong and F. Schmidt, *Large-scale galaxy bias*, *Phys. Rep.* **733** (2018) 1 [[1611.09787](#)].
- [63] V. Desjacques, D. Jeong and F. Schmidt, *The Galaxy Power Spectrum and Bispectrum in Redshift Space*, *JCAP* **12** (2018) 035 [[1806.04015](#)].
- [64] T. Lazeyras and F. Schmidt, *Beyond LIMD bias: a measurement of the complete set of third-order halo bias parameters*, *Journal of Cosmology and Astro-Particle Physics* **2018** (2018) 008 [[1712.07531](#)].
- [65] V. Desjacques and U. Seljak, *Primordial Non-Gaussianity in the Large-Scale Structure of the Universe*, *Advances in Astronomy* **2010** (2010) 908640 [[1006.4763](#)].
- [66] F. Schmidt and M. Kamionkowski, *Halo clustering with nonlocal non-Gaussianity*, *Phys. Rev. D* **82** (2010) 103002 [[1008.0638](#)].
- [67] R. Scoccimarro, L. Hui, M. Manera and K. C. Chan, *Large-scale bias and efficient generation of initial conditions for nonlocal primordial non-Gaussianity*, *Phys. Rev. D* **85** (2012) 083002 [[1108.5512](#)].
- [68] V. Desjacques, D. Jeong and F. Schmidt, *Accurate predictions for the scale-dependent galaxy bias from primordial non-Gaussianity*, *Phys. Rev. D* **84** (2011) 061301 [[1105.3476](#)].

- [69] F. Schmidt, D. Jeong and V. Desjacques, *Peak-background split, renormalization, and galaxy clustering*, *Phys. Rev. D* **88** (2013) 023515 [[1212.0868](#)].
- [70] P. McDonald, *Primordial non-Gaussianity: Large-scale structure signature in the perturbative bias model*, *Phys. Rev. D* **78** (2008) 123519 [[0806.1061](#)].
- [71] T. Giannantonio and C. Porciani, *Structure formation from non-Gaussian initial conditions: Multivariate biasing, statistics, and comparison with N-body simulations*, *Phys. Rev. D* **81** (2010) 063530 [[0911.0017](#)].
- [72] T. Baldauf, U. Seljak and L. Senatore, *Primordial non-Gaussianity in the bispectrum of the halo density field*, *Journal of Cosmology and Astro-Particle Physics* **4** (2011) 006 [[1011.1513](#)].
- [73] V. Assassi, D. Baumann and F. Schmidt, *Galaxy bias and primordial non-Gaussianity*, *Journal of Cosmology and Astro-Particle Physics* **12** (2015) 043 [[1510.03723](#)].
- [74] W. H. Press and P. Schechter, *Formation of Galaxies and Clusters of Galaxies by Self-Similar Gravitational Condensation*, *ApJ* **187** (1974) 425.
- [75] J. Tinker, A. V. Kravtsov, A. Klypin, K. Abazajian, M. Warren, G. Yepes et al., *Toward a Halo Mass Function for Precision Cosmology: The Limits of Universality*, *ApJ* **688** (2008) 709 [[0803.2706](#)].
- [76] V. Desjacques, D. Jeong and F. Schmidt, *Non-Gaussian Halo Bias Re-examined: Mass-dependent Amplitude from the Peak-Background Split and Thresholding*, *Phys. Rev. D* **84** (2011) 063512 [[1105.3628](#)].
- [77] E. Sefusatti, M. Crocce and V. Desjacques, *The halo bispectrum in N-body simulations with non-Gaussian initial conditions*, *MNRAS* **425** (2012) 2903 [[1111.6966](#)].
- [78] T. Giannantonio, C. Porciani, J. Carron, A. Amara and A. Pillepich, *Constraining primordial non-Gaussianity with future galaxy surveys*, *MNRAS* **422** (2012) 2854 [[1109.0958](#)].
- [79] M. LoVerde, A. Miller, S. Shandera and L. Verde, *Effects of scale-dependent non-Gaussianity on cosmological structures*, *Journal of Cosmology and Astro-Particle Physics* **4** (2008) 014 [[0711.4126](#)].
- [80] V. Desjacques, U. Seljak and I. T. Iliev, *Scale-dependent bias induced by local non-Gaussianity: a comparison to N-body simulations*, *MNRAS* **396** (2009) 85 [[0811.2748](#)].
- [81] U. Seljak, *Analytic model for galaxy and dark matter clustering*, *Mon. Not. Roy. Astron. Soc.* **318** (2000) 203 [[astro-ph/0001493](#)].
- [82] J. Peacock and R. Smith, *Halo occupation numbers and galaxy bias*, *Mon. Not. Roy. Astron. Soc.* **318** (2000) 1144 [[astro-ph/0005010](#)].
- [83] R. Scoccimarro, R. K. Sheth, L. Hui and B. Jain, *How many galaxies fit in a halo? Constraints on galaxy formation efficiency from spatial clustering*, *Astrophys. J.* **546** (2001) 20 [[astro-ph/0006319](#)].
- [84] F. Villaescusa-Navarro, M. Viel, K. K. Datta and T. R. Choudhury, *Modeling the neutral hydrogen distribution in the post-reionization Universe: intensity mapping*, *JCAP* **09** (2014) 050 [[1405.6713](#)].
- [85] E. Castorina and F. Villaescusa-Navarro, *On the spatial distribution of neutral hydrogen in the Universe: bias and shot-noise of the H I power spectrum*, *MNRAS* **471** (2017) 1788 [[1609.05157](#)].
- [86] J. L. Tinker, B. E. Robertson, A. V. Kravtsov, A. Klypin, M. S. Warren, G. Yepes et al., *The Large-scale Bias of Dark Matter Halos: Numerical Calibration and Model Tests*, *ApJ* **724** (2010) 878 [[1001.3162](#)].

- [87] T. Lazeyras, C. Wagner, T. Baldauf and F. Schmidt, *Precision measurement of the local bias of dark matter halos*, *Journal of Cosmology and Astro-Particle Physics* **2016** (2016) 018 [[1511.01096](#)].
- [88] R. K. Sheth and G. Tormen, *Large-scale bias and the peak background split*, *MNRAS* **308** (1999) 119 [[astro-ph/9901122](#)].
- [89] H. Padmanabhan and A. Refregier, *Constraining a halo model for cosmological neutral hydrogen*, *MNRAS* **464** (2017) 4008 [[1607.01021](#)].
- [90] H. Padmanabhan, A. Refregier and A. Amara, *A halo model for cosmological neutral hydrogen : abundances and clustering*, *MNRAS* **469** (2017) 2323 [[1611.06235](#)].
- [91] W. L. W. Sargent and E. L. Turner, *A statistical method for determining the cosmological density parameter from the redshifts of a complete sample of galaxies*, *Astrophys. J.* **212** (1977) L3.
- [92] N. Kaiser, *Clustering in real space and in redshift space*, *MNRAS* **227** (1987) 1.
- [93] A. J. S. Hamilton, *Linear Redshift Distortions: a Review*, in *The Evolving Universe* (D. Hamilton, ed.), vol. 231 of *Astrophysics and Space Science Library*, p. 185, 1998, [astro-ph/9708102](#), DOI.
- [94] L. Verde, A. F. Heavens, S. Matarrese and L. Moscardini, *Large-scale bias in the Universe - II. Redshift-space bispectrum*, *MNRAS* **300** (1998) 747 [[astro-ph/9806028](#)].
- [95] R. Scoccimarro, S. Colombi, J. N. Fry, J. A. Frieman, E. Hivon and A. Melott, *Nonlinear Evolution of the Bispectrum of Cosmological Perturbations*, *ApJ* **496** (1998) 586 [[astro-ph/9704075](#)].
- [96] J. C. Jackson, *A critique of Rees's theory of primordial gravitational radiation*, *MNRAS* **156** (1972) 1P [[0810.3908](#)].
- [97] H. Gil-Marín, J. Noreña, L. Verde, W. J. Percival, C. Wagner, M. Manera et al., *The power spectrum and bispectrum of SDSS DR11 BOSS galaxies – I. Bias and gravity*, *Mon. Not. Roy. Astron. Soc.* **451** (2015) 539 [[1407.5668](#)].
- [98] I. Hashimoto, Y. Rasera and A. Taruya, *Precision cosmology with redshift-space bispectrum: a perturbation theory based model at one-loop order*, *Phys. Rev. D* **96** (2017) 043526 [[1705.02574](#)].
- [99] A. Lazanu and M. Liguori, *The two and three-loop matter bispectrum in perturbation theories*, *JCAP* **04** (2018) 055 [[1803.03184](#)].
- [100] A. Oddo, E. Sefusatti, C. Porciani, P. Monaco and A. G. Sánchez, *Toward a robust inference method for the galaxy bispectrum: likelihood function and model selection*, *JCAP* **03** (2020) 056 [[1908.01774](#)].
- [101] R. Scoccimarro, H. M. P. Couchman and J. A. Frieman, *The Bispectrum as a Signature of Gravitational Instability in Redshift Space*, *ApJ* **517** (1999) 531 [[astro-ph/9808305](#)].
- [102] Cosmic Visions 21 cm Collaboration, R. Ansari, E. J. Arena, K. Bandura, P. Bull, E. Castorina et al., *Inflation and Early Dark Energy with a Stage II Hydrogen Intensity Mapping Experiment*, *arXiv e-prints* (2018) arXiv:1810.09572 [[1810.09572](#)].
- [103] F. Schmidt, *Towards a self-consistent halo model for the nonlinear large-scale structure*, *Phys. Rev. D* **93** (2016) 063512 [[1511.02231](#)].
- [104] D. Bertacca, A. Raccanelli, N. Bartolo, M. Liguori, S. Matarrese and L. Verde, *Relativistic wide-angle galaxy bispectrum on the light cone*, *Phys. Rev. D* **97** (2018) 023531 [[1705.09306](#)].
- [105] M. Zaldarriaga, S. R. Furlanetto and L. Hernquist, *21 Centimeter Fluctuations from Cosmic Gas at High Redshifts*, *ApJ* **608** (2004) 622 [[astro-ph/0311514](#)].

- [106] M. Tegmark and M. Zaldarriaga, *Fast Fourier transform telescope*, *Phys. Rev. D* **79** (2009) 083530 [0805.4414].
- [107] L. B. Newburgh, G. E. Addison, M. Amiri, K. Bandura, J. R. Bond, L. Connor et al., *Calibrating CHIME: a new radio interferometer to probe dark energy*, in Proc. SPIE, vol. 9145 of *Society of Photo-Optical Instrumentation Engineers (SPIE) Conference Series*, p. 91454V, Jul, 2014, 1406.2267, DOI.
- [108] L. B. Newburgh, K. Bandura, M. A. Bucher, T. C. Chang, H. C. Chiang, J. F. Cliche et al., *HIRAX: a probe of dark energy and radio transients*, in Proc. SPIE, vol. 9906 of *Society of Photo-Optical Instrumentation Engineers (SPIE) Conference Series*, p. 99065X, Aug, 2016, 1607.02059, DOI.
- [109] A. Poursidou, *Synergistic tests of inflation*, 1612.05138.
- [110] J. Shaw, K. Sigurdson, U.-L. Pen, A. Stebbins and M. Sitwell, *All-Sky Interferometry with Spherical Harmonic Transit Telescopes*, *Astrophys. J.* **781** (2014) 57 [1302.0327].
- [111] J. Shaw, K. Sigurdson, M. Sitwell, A. Stebbins and U.-L. Pen, *Coaxing cosmic 21 cm fluctuations from the polarized sky using m-mode analysis*, *Phys. Rev. D* **91** (2015) 083514 [1401.2095].
- [112] J. C. Pober, *The Impact of Foregrounds on Redshift Space Distortion Measurements With the Highly-Redshifted 21 cm Line*, *Mon. Not. Roy. Astron. Soc.* **447** (2015) 1705 [1411.2050].
- [113] R. Byrne, M. F. Morales, B. Hazelton, W. Li, N. Barry, A. P. Beardsley et al., *Fundamental Limitations on the Calibration of Redundant 21 cm Cosmology Instruments and Implications for HERA and the SKA*, *Astrophys. J.* **875** (2019) 70 [1811.01378].
- [114] T. Jacobson and R. Parentani, *Horizon entropy*, *Found. Phys.* **33** (2003) 323 [gr-qc/0302099].
- [115] S. Furlanetto, S. Oh and F. Briggs, *Cosmology at Low Frequencies: The 21 cm Transition and the High-Redshift Universe*, *Phys. Rept.* **433** (2006) 181 [astro-ph/0608032].
- [116] A. Liu and M. Tegmark, *A method for 21 cm power spectrum estimation in the presence of foregrounds*, *Phys. Rev. D* **83** (2011) 103006 [1103.0281].
- [117] A. Liu and M. Tegmark, *How well can we measure and understand foregrounds with 21-cm experiments?*, *MNRAS* **419** (2012) 3491 [1106.0007].
- [118] J. Jasche and F. S. Kitaura, *Fast Hamiltonian sampling for large-scale structure inference*, *MNRAS* **407** (2010) 29 [0911.2496].
- [119] F. S. Kitaura, *The initial conditions of the universe from constrained simulations.*, *MNRAS* **429** (2013) L84 [1203.4184].
- [120] H. Wang, H. Mo, X. Yang, Y. Jing and W. Lin, *ELUCID - Exploring the Local Universe with reConstructed Initial Density field I: Hamiltonian Markov Chain Monte Carlo Method with Particle Mesh Dynamics*, *Astrophys. J.* **794** (2014) 94 [1407.3451].
- [121] J. Jasche, F. Leclercq and B. D. Wandelt, *Past and present cosmic structure in the SDSS DR7 main sample*, *JCAP* **01** (2015) 036 [1409.6308].
- [122] H. Wang, H. Mo, X. Yang, Y. Zhang, J. Shi, Y. Jing et al., *ELUCID - Exploring the Local Universe with reConstructed Initial Density field III: Constrained Simulation in the SDSS Volume*, *Astrophys. J.* **831** (2016) 164 [1608.01763].
- [123] U. Seljak, G. Aslanyan, Y. Feng and C. Modi, *Towards optimal extraction of cosmological information from nonlinear data*, *JCAP* **12** (2017) 009 [1706.06645].
- [124] C. Modi, Y. Feng and U. Seljak, *Cosmological Reconstruction From Galaxy Light: Neural Network Based Light-Matter Connection*, *JCAP* **10** (2018) 028 [1805.02247].
- [125] H.-M. Zhu, U.-L. Pen, Y. Yu and X. Chen, *Recovering lost 21 cm radial modes via cosmic tidal reconstruction*, *Phys. Rev. D* **98** (2018) 043511 [1610.07062].

- [126] N. G. Karaçaylı and N. Padmanabhan, *Anatomy of Cosmic Tidal Reconstruction*, *Mon. Not. Roy. Astron. Soc.* **486** (2019) 3864 [[1904.01387](#)].
- [127] C. Modi, M. White, A. Slosar and E. Castorina, *Reconstructing large-scale structure with neutral hydrogen surveys*, *JCAP* **11** (2019) 023 [[1907.02330](#)].
- [128] J. C. Pober, A. Liu, J. S. Dillon, J. E. Aguirre, J. D. Bowman, R. F. Bradley et al., *What Next-generation 21 cm Power Spectrum Measurements can Teach us About the Epoch of Reionization*, *ApJ* **782** (2014) 66 [[1310.7031](#)].
- [129] J. C. Pober, *The impact of foregrounds on redshift space distortion measurements with the highly redshifted 21-cm line*, *MNRAS* **447** (2015) 1705 [[1411.2050](#)].
- [130] R. Scoccimarro, E. Sefusatti and M. Zaldarriaga, *Probing primordial non-Gaussianity with large-scale structure*, *Phys. Rev. D* **69** (2004) 103513 [[astro-ph/0312286](#)].
- [131] E. Sefusatti, M. Crocce, S. Pueblas and R. Scoccimarro, *Cosmology and the bispectrum*, *Phys. Rev. D* **74** (2006) 023522 [[astro-ph/0604505](#)].
- [132] E. Sefusatti and E. Komatsu, *Bispectrum of galaxies from high-redshift galaxy surveys: Primordial non-Gaussianity and nonlinear galaxy bias*, *Phys. Rev. D* **76** (2007) 083004 [[0705.0343](#)].
- [133] K. C. Chan and L. Blot, *Assessment of the information content of the power spectrum and bispectrum*, *Phys. Rev. D* **96** (2017) 023528 [[1610.06585](#)].
- [134] R. E. Smith, J. A. Peacock, A. Jenkins, S. D. M. White, C. S. Frenk, F. R. Pearce et al., *Stable clustering, the halo model and non-linear cosmological power spectra*, *MNRAS* **341** (2003) 1311 [[astro-ph/0207664](#)].
- [135] R. Takahashi, M. Sato, T. Nishimichi, A. Taruya and M. Oguri, *Revising the Halofit Model for the Nonlinear Matter Power Spectrum*, *ApJ* **761** (2012) 152 [[1208.2701](#)].
- [136] Y. Wang, *Dark Energy Constraints from Baryon Acoustic Oscillations*, *ApJ* **647** (2006) 1 [[astro-ph/0601163](#)].
- [137] M. Liguori and A. Riotto, *Impact of uncertainties in the cosmological parameters on the measurement of primordial non-Gaussianity*, *Phys. Rev. D* **78** (2008) 123004 [[0808.3255](#)].
- [138] A. Moradinezhad Dizgah, H. Lee, J. B. Muñoz and C. Dvorkin, *Galaxy Bispectrum from Massive Spinning Particles*, *ArXiv e-prints* (2018) [[1801.07265](#)].
- [139] N. Bellomo, J. L. Bernal, G. Scelfo, A. Raccanelli and L. Verde, *Beware of commonly used approximations I: errors in forecasts*, [2005.10384](#).
- [140] N. Agarwal, V. Desjacques, D. Jeong and F. Schmidt, *Information content in the redshift-space galaxy power spectrum and bispectrum*, [2007.04340](#).
- [141] T. Baldauf, M. Mirbabayi, M. Simonović and M. Zaldarriaga, *LSS constraints with controlled theoretical uncertainties*, *ArXiv e-prints* (2016) [[1602.00674](#)].
- [142] P. Bull, P. G. Ferreira, P. Patel and M. G. Santos, *Late-time Cosmology with 21 cm Intensity Mapping Experiments*, *ApJ* **803** (2015) 21 [[1405.1452](#)].
- [143] C. A. Watkinson, C. M. Trott and I. Hothi, *The bispectrum and 21cm foregrounds during the Epoch of Reionization*, [2002.05992](#).
- [144] Planck Collaboration, P. A. R. Ade, N. Aghanim, M. Arnaud, F. Arroja, M. Ashdown et al., *Planck 2015 results. XVII. Constraints on primordial non-Gaussianity*, *A&A* **594** (2016) A17 [[1502.01592](#)].
- [145] O. Doré, J. Bock, M. Ashby, P. Capak, A. Cooray, R. de Putter et al., *Cosmology with the SPHEREX All-Sky Spectral Survey*, *ArXiv e-prints* (2014) [[1412.4872](#)].

- [146] M. Tellarini, A. J. Ross, G. Tasinato and D. Wands, *Galaxy bispectrum, primordial non-Gaussianity and redshift space distortions*, *Journal of Cosmology and Astro-Particle Physics* **6** (2016) 014 [1603.06814].
- [147] J. A. Peacock and S. J. Dodds, *Reconstructing the Linear Power Spectrum of Cosmological Mass Fluctuations*, *MNRAS* **267** (1994) 1020 [astro-ph/9311057].
- [148] W. E. Ballinger, J. A. Peacock and A. F. Heavens, *Measuring the cosmological constant with redshift surveys*, *MNRAS* **282** (1996) 877 [astro-ph/9605017].

A Derivation of Bias Parameters from the Tinker et al mass function with the PBS approach

The peak-background split (PBS) approach (see e.g. Ref. [62] for a review) derives the halo bias parameters from the change in the distribution of the density peaks (i.e. the mass function). The density fluctuation field can be decomposed into a long-wavelength linear fluctuation, $\delta_l(\mathbf{x})$, and a noisy short wavelength one, $\delta_s(\mathbf{x})$. The first will modulate the background density and alter the height of the peaks to an effective value

$$\nu \rightarrow \nu_{\text{eff}} = \frac{\delta_c - \delta_l}{\sigma_R}. \quad (\text{A.1})$$

The halo number density in Lagrangian coordinates is given by (see e.g. Appendix C of Ref. [22])

$$\delta_h^L(M|M_1, V_0) = \frac{n_h(M|M_1, V_0, z)}{n_h(M, z)} - 1. \quad (\text{A.2})$$

where $n_h(M|M_1, V_0)$ is the number of subhalos of mass M with an initial volume V_0 , corresponding to the small wavelength peaks ready to collapse on top of the long mode, above some mass M_1 defined by the “background” (i.e. long wavelength) mode and $n_h(M, z)$ is the mean number of halos above mass M (i.e. the halo mass function). Taylor expanding Eq. (A.2) and comparing it with the local-in-matter bias expansion, we can identify the Lagrangian bias coefficients as

$$b_N^L(M, z) = \frac{1}{n_h(M, z)} \left. \frac{\partial^N n_h(M, z)}{\partial \delta_l^N} \right|_{\delta_l=0} = \frac{(-\nu)^N}{\delta_c^N f(\nu, z)} \frac{d^N f(\nu, z)}{d\nu^N}. \quad (\text{A.3})$$

This is a general result for any universal mass function, therefore we can use it to derive the halo bias parameters for the fitting mass function of Ref. [75], given by

$$f(\nu, z) = \alpha \left[1 + (\beta\nu)^{-2\phi} \right] \nu^{2\eta} e^{-\gamma\nu^2/2}, \quad (\text{A.4})$$

where the parameters have the following redshift dependence

$$\beta(z) = \beta_0(1+z)^{0.2}, \quad (\text{A.5})$$

$$\phi = \phi_0(1+z)^{-0.08}, \quad (\text{A.6})$$

$$\eta = \eta_0(1+z)^{0.27}, \quad (\text{A.7})$$

$$\gamma = \gamma_0(1+z)^{-0.01}, \quad (\text{A.8})$$

where the zero in the subscript denotes the values of the fitting parameters for $z = 0$ and can be found in Table 4 of Ref. [86], together with amplitude α values.

The first four local-in-matter Lagrangian halo bias parameters are

$$b_1^L = \frac{2\varphi}{\delta_c [(\beta\nu)^{2\varphi} + 1]} + \frac{\gamma\nu^2 - 2\eta - 1}{\delta_c}, \quad (\text{A.9})$$

$$b_2^L = \frac{2\varphi (2\gamma\nu^2 - 4\eta + 2\varphi - 1)}{\delta_c^2 [(\beta\nu)^{2\varphi} + 1]} + \frac{\gamma^2\nu^4 - 4\gamma\eta\nu^2 - 3\gamma\nu^2 + 4\eta^2 + 2\eta}{\delta_c^2}, \quad (\text{A.10})$$

$$b_3^L = \frac{2\varphi (6\varphi (\gamma\nu^2 - 2\eta) + 3 (\gamma\nu^2 - 2\eta)^2 - 6\gamma\nu^2 + 4\varphi^2 - 1)}{\delta_c^3 [(\beta\nu)^{2\varphi} + 1]} + \frac{\gamma^3\nu^6 - 6\gamma^2\eta\nu^4 - 6\gamma^2\nu^4 + 12\gamma\eta^2\nu^2 + 12\gamma\eta\nu^2 + 3\gamma\nu^2 - 8\eta^3 + 2\eta}{\delta_c^3}, \quad (\text{A.11})$$

$$b_4^L = \frac{4\varphi}{\delta_c^4 [(\beta\nu)^{2\varphi} + 1]} [2\gamma^3\nu^6 - 2\eta (6\gamma^2\nu^4 + 6\gamma\nu^2(2\varphi - 1) + 8\varphi^2 + 6\varphi - 1) + 3\gamma^2\nu^4(2\varphi - 3) + 12\eta^2 (2\gamma\nu^2 + 2\varphi + 1) + \gamma\nu^2 (8\varphi^2 - 6\varphi + 1) - 16\eta^3 + 4\varphi^2(\varphi + 1) - \varphi - 1] + \frac{\gamma^4\nu^8 - 8\gamma^3\eta\nu^6 - 10\gamma^3\nu^6 + 24\gamma^2\eta^2\nu^4 + 36\gamma^2\eta\nu^4 + 15\gamma^2\nu^4}{\delta_c^4} + \frac{-32\gamma\eta^3\nu^2 - 24\gamma\eta^2\nu^2 - 4\gamma\eta\nu^2 + 16\eta^4 - 16\eta^3 - 4\eta^2 + 4\eta}{\delta_c^4}. \quad (\text{A.12})$$

From the mapping between Eulerian and Lagrangian bias in the spherical collapse approximation, we get ³

$$b_1^E = 1 + b_1^L, \quad (\text{A.13})$$

$$b_2^E = b_2^L + 2(\alpha_1 + \alpha_2)b_1^L, \quad (\text{A.14})$$

$$b_3^E = 6(\alpha_2 + \alpha_3)b_1^L + 3(1 + 2\alpha_2)b_2^L + b_3^L, \quad (\text{A.15})$$

$$b_4^E = 24(\alpha_3 + \alpha_4)b_1^L + 12(\alpha_2^2 + 2(\alpha_2 + \alpha_3))b_2^L + 4(1 + 3\alpha_2)b_3^L + b_4^L. \quad (\text{A.16})$$

where $\alpha_1 = 1$, $\alpha_2 = -17/21$, $\alpha_3 = 2815/3969$ and $\alpha_4 = -590725/916839$.

The resulting Eulerian HI bias parameters, after using the methodology and HOD model described in Sec. 2.3, are plotted in Fig. 3.

B Baseline distribution

Accurate modeling of the effective distribution of baselines is non-trivial for transit telescopes. The sky rotation that takes objects over the sky has the effect that the same piece of sky is measured by the same baseline with different projection and the m -mode analysis (cite) demonstrates that some information that is not sampled directly can be recovered through time variation. In particular, for experiments like HIRAX, different patches of the sky will be observed with different pointing altitudes and PUMA will also likely to have at least one degree of freedom per dish. We skim over these details and use smoothed version of physical distribution of baseline lengths instead.

³See e.g. Appendix C of Ref. [22] for more details.

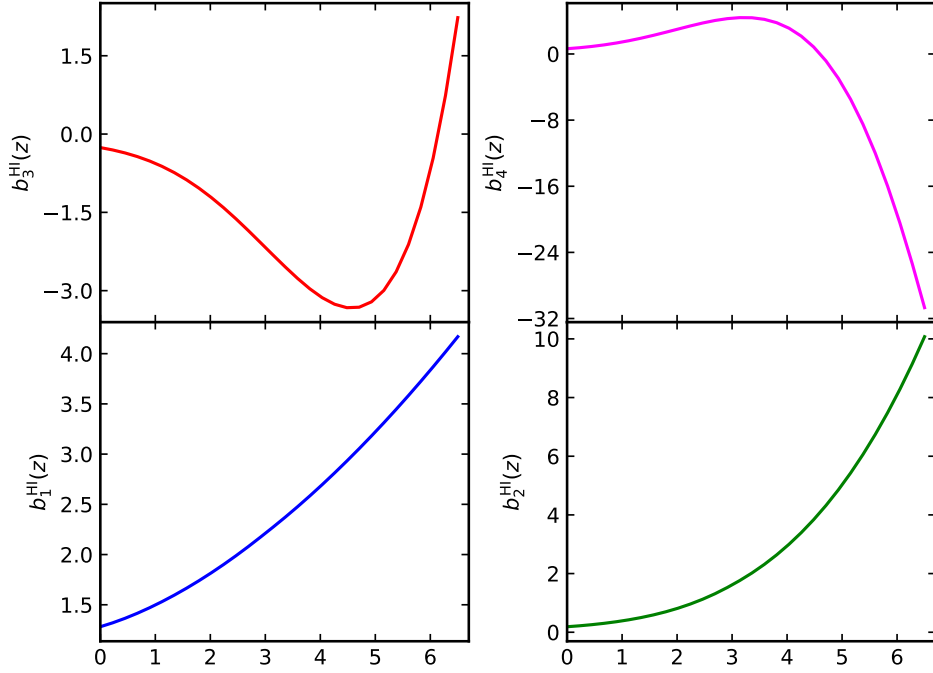


Figure 3. The first four local-in-matter Eulerian bias parameters of the HI galaxies [Eq. (2.16)] as a function of redshift. The derivation uses the HOD model of Ref. [85], which is briefly described in Sec. 2.3.

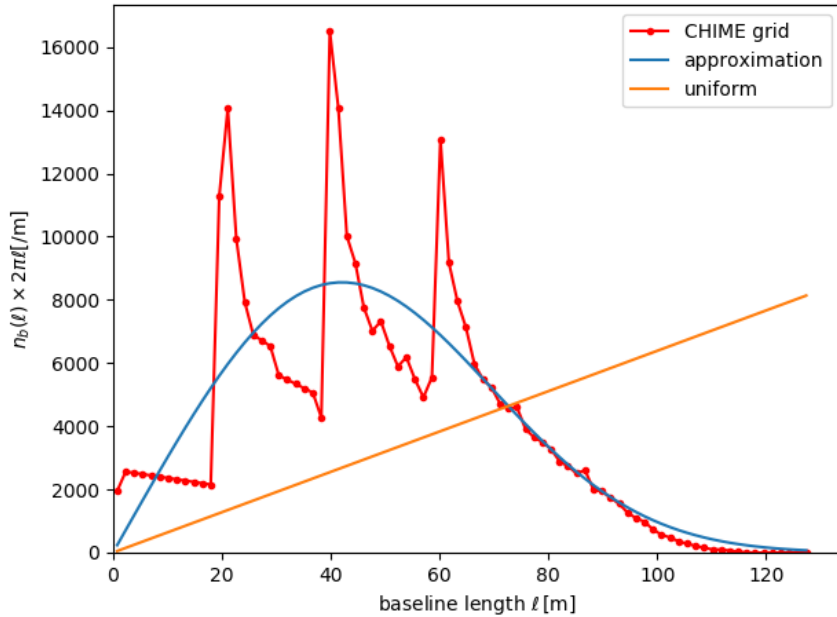


Figure 4. A comparison of the CHIME baseline distribution with the approximating formula of Eq. (B.2) and the uniform distribution, which assumes a constant sampling in the u - v plane (see e.g. Ref. [142]).

The baseline distribution for the PUMA and HIRAX surveys is given by Eq. D4 of [102], given by the following fitting formula

$$n_b(l) = n_0 \frac{a + b(l/L)}{1 + c(l/L)^d} e^{-(l/L)^e}, \quad (\text{B.1})$$

where $n_0 = (N_s/D_{\text{dish}})^2$ and $L = N_s D_{\text{dish}}$ with $n_b(u) = n_b(l = u\lambda)\lambda^2$, while N_s is the number of antennas in the side of the square array (i.e. $N_s = 256$ for PUMA and $N_s = 32$ for HIRAX). This formula has been calibrated so that $\int n_b(u) d^2u = N_s^2/2$. The fitting parameters for a square closed-packing array, considered in the case of HIRAX, are $a = 0.4847$, $b = -0.3300$, $c = 1.3157$, $d = 1.5974$, $e = 6.8390$. For PUMA, as discussed in the main text, we consider a hexagonal closed-packing array in a compact cycle, where the fitting parameters are now $a = 0.5698$, $b = -0.5274$, $c = 0.8358$, $d = 1.6635$, $e = 7.3177$. For both cases, the fitted parameters can be found in Appendix D of Ref. [102], as well as a detailed discussion.

For CHIME the baseline distribution is given by the following fitting formula

$$n_b(l) = A \exp[-(l/B)^C], \quad (\text{B.2})$$

where the parameters are, $A = 48.5511$, $B = 60.693$, $C = 2.4797$. A comparison between the actual baseline length distribution for CHIME and the fitting formula is shown in Fig. 4.

C Redshift space kernels and the Finger-of-God dumping term

The effect of redshift space distortions (RSD) [92, 93] can be treated perturbatively [94, 101], generalising the kernel formalism of SPT in order to include the redshift distortions and the bias terms [Eqs. (2.9) and (2.10)]. The general non-Gaussian redshift kernels up to second order, while neglecting $\mathcal{O}(f_{\text{NL}}^2)$ terms, are given by (see e.g. Refs. [22, 72, 146]):

$$Z_1(\mathbf{k}_i) = b_1 + f\mu_i^2 + \frac{b_\Psi k_i^\alpha}{M(k_i, z)}, \quad (\text{C.1})$$

$$\begin{aligned} Z_2(\mathbf{k}_i, \mathbf{k}_j) &= b_1 F_2(\mathbf{k}_i, \mathbf{k}_j) + f\mu_{ij}^2 G_2(\mathbf{k}_i, \mathbf{k}_j) + \frac{b_2}{2} + b_{s2} S_2(\mathbf{k}_i, \mathbf{k}_j) \\ &+ \frac{f\mu_{ij} k_{ij}}{2} \left[\frac{\mu_i}{k_i} Z_1(\mathbf{k}_j) + \frac{\mu_j}{k_j} Z_1(\mathbf{k}_i) \right] + \frac{1}{2} \left(\frac{(b_{\Psi\delta} - b_\Psi N_2(\mathbf{k}_j, \mathbf{k}_i)) k_i^\alpha}{M(k_i, z)} + \frac{(b_{\Psi\delta} - b_\Psi N_2(\mathbf{k}_i, \mathbf{k}_j)) k_j^\alpha}{M(k_j, z)} \right), \end{aligned} \quad (\text{C.2})$$

where f is the linear growth rate, $\mu_i = \mathbf{k}_i \cdot \hat{z}/k_i$ is the cosine of the angle between the wavevector \mathbf{k}_i and the line-of-sight \hat{z} , $\mu_{ij} = (\mu_i k_i + \mu_j k_j)/k_{ij}$ and $k_{ij}^2 = (\mathbf{k}_i + \mathbf{k}_j)^2$. The kernels $F_2(\mathbf{k}_i, \mathbf{k}_j)$ and $G_2(\mathbf{k}_i, \mathbf{k}_j)$ are the second order symmetric kernels of SPT (see Ref. [46] for a review), while $S_2(\mathbf{k}_1, \mathbf{k}_2) = (\mathbf{k}_1 \cdot \mathbf{k}_2)^2 / (k_1^2 k_2^2) - 1/3$ and $N_2(\mathbf{k}_1, \mathbf{k}_2) = (\mathbf{k}_1 \cdot \mathbf{k}_2) / (k_1^2)$. The S_2 kernel arises from the Fourier transform of the tidal field scalar s^2 [52, 55], while N_2 , in the presence of PNG, originates from the coupling of the displacement field between the Eulerian and Lagrangian frames to the primordial gravitational potential [71, 72]. For the different PNG shapes considered here, parameter α get the following values: $\alpha = 2$ for the equilateral shape, $\alpha = 1$ for the orthogonal configuration, while the usual local case can be retrieved by $\alpha = 0$ [16, 28, 71]. Note that in the expressions above, the redshift dependence has been suppressed for clarity.

The Finger-of-God (FOG) is taken into account here, where the damping effect of the clustering power is described phenomenologically by [147, 148]

$$D_{\text{FOG}}^P(\mathbf{k}) = e^{-(k\mu\sigma_P)^2}, \quad (\text{C.3})$$

$$D_{\text{FOG}}^B(\mathbf{k}_1, \mathbf{k}_2, \mathbf{k}_3) = e^{-(k_1^2\mu_1^2 + k_2^2\mu_2^2 + k_3^2\mu_3^2)\sigma_B^2}. \quad (\text{C.4})$$

Here we consider the fiducial values for $\sigma_P = \sigma_B = \sigma_v(z)$, where σ_v is the usual linear, one dimensional velocity dispersion. Note that, due to the high precision of the redshift measurements in 21 cm IM surveys considered here, the redshift error is assumed to be zero, i.e. perfect knowledge of redshift.